

**Tracking of Manifolds and Coherent Structures in Flows:
Simulations and Experiments**

A Thesis

Submitted to the Faculty

of

Drexel University

by

Matt Michini

in partial fulfillment of the
requirements for the degree

of

Master of Science in Mechanical Engineering and Mechanics

June 2014

© Copyright June 2014
Matt Michini. All Rights Reserved.

Acknowledgements

I would like to first acknowledge my advisor and mentor, Dr. Ani Hsieh, for her support and guidance throughout the course of this work and for fostering and encouraging my growth as a student and engineer over the past two years. In addition, I would like to extend thanks to Dr. Eric Forgoston, Dr. Ira Schwartz, Dr. Phil Yecko, Hossein Rastgoftar, and Dr. Suhada Jayasuriya, with whom it has been a pleasure to collaborate. Thanks are due to Alex Abad, Stef Teleski, and Zach Block for their help, and to my lab mates at the Scalable Autonomous Systems lab, namely Den, Ken, James, John, Milligan, and Bill.

This thesis is based upon work supported by the Office of Naval Research under Contract Number N0001411WX20079.

Dedications

To my family, for their endless support and encouragement.

Table of Contents

List of Figures	iii
Abstract	vi
1. Introduction	1
1.1 Motivation	1
1.2 Related Work	3
1.3 Contributions of this Thesis	3
1.4 Overview	4
2. Background	5
2.1 Kinematics Model	5
2.2 Flow Models	6
2.3 Ocean Model	7
2.4 Finite-time Lyapunov Exponents (FTLE)	8
2.4.1 Computation of the FTLE	9
2.4.2 Computation of FTLE Field using Discrete Flow Velocity Data	10
2.5 Lagrangian Coherent Structures (LCS)	12
2.6 Summary	13
3. Manifold and Coherent Structure Tracking Strategies	14
3.1 Three Robot LCS Tracking Strategy	14
3.2 LCS Tracking with Formation Control	17
3.3 Summary	18
4. Experimental Testbed	19
4.1 Autonomous Surface Vehicles (ASVs)	19
4.1.1 Design of the Vehicles	19
4.1.2 Custom Controller Board	21
4.1.3 Flow Sensor Design (mASVF)	23
4.2 Flow Tanks	27
4.2.1 LoRe Tank	29
4.2.2 HiRe Tank	29
4.2.3 Multi-Robot (MR) Tank	32
4.3 Summary	32

5.	Simulation Results.....	33
5.1	Methodology and Implementation.....	33
5.2	Tracking with the Wind-Driven Double Gyre Model	33
5.2.1	Static Double Gyre Model	33
5.2.2	Time Varying Double Gyre Model	34
5.2.3	Modeling Sensor Noise	35
5.3	Tracking with Formation Control	35
5.4	Tracking using HiRe Tank Data.....	37
5.5	Tracking using Ocean Flow Data.....	39
5.6	Summary	40
6.	Experimental Results	41
6.1	MR Tank - Still Water	41
6.1.1	Static Double Gyre Model	41
6.1.2	Time Varying Double Gyre Model	43
6.1.3	Scaled-up HiRe Tank Data	45
6.1.4	Double Gyre Model with Larger Teams	45
6.2	MR Tank - Generated Flow	45
6.3	Summary	46
7.	Conclusion	48
7.1	Summary of Contributions.....	48
7.2	Future Work	48
7.2.1	Simulations	49
7.2.2	Experiments	50
	Bibliography	52

List of Figures

2.1	Phase portrait for the model given by (2.3) with $A = 1$, $\mu = 0$, $\varepsilon = 0$, $\psi = 0$, and $s = 1$...	6
2.2	Sample high-frequency (HF) radar derived hourly coastal ocean current data from the Southern California Coastal Ocean Observing System.	7
2.3	Diagram illustrating the initial and final locations of 4 advected particles in a flow.	9
2.4	(a) Static double gyre vector field and (b) corresponding FTLE field for (2.4) with $A = 1$ and $s = 1$	10
2.5	(a) Sample HF radar derived ocean current data for the Santa Barbara Channel and (b) corresponding FTLE field, computed with an integration time of 24 hours.....	11
2.6	Phase portrait of a simple pendulum.	12
3.1	An errant case illustrating the need for $d_{Max} < \rho_{min}(B_*)$. Here, L and R , traversing from left to right, end up on the same side of the boundary and no longer form a valid saddle straddling line segment.	16
3.2	Diagram of the 3-agent tracking strategy. The current saddle-straddling line segment J_{t_0} is indicated by a solid red line, and the projected straddling line segment $J_{t_0 + \Delta T}$ is indicated by a solid blue line. The vertices of the red triangle are thus the current positions of the robots, and those of the blue triangle are the desired positions after time ΔT	18
4.1	Examples of the two classes of autonomous surface vehicles used for this work, with and without 3D printed cap. Pictured on the left are the mASVs, and on the right are the mASVFs with flow sensors.	20
4.2	(a) 3D CAD model of an mASV and (b) photo of 3 mASVs.	21
4.3	Custom controller board for the mASVs. Each board includes an 8-bit microcontroller, a 6-axis acceleration and angular rate sensor, and 2 motor controller ICs.	22
4.4	Inside view of the mASVF in the MR tank (a) without and (b) with unique pattern of retro-reflective markers.	23
4.5	Unfiltered encoder angle data (black) and low-pass filtered data (red).	24
4.6	Free body diagram for the sensor rod, where the horizontal dashed line indicates water free surface level.	25
4.7	(a) Diagram of mASV in global XY frame. (b) Top view photos of a typical mASV demonstrating the locations of the two flow sensing encoders and retro-reflective markers.	26

4.8 (a) Encoder A angular displacement vs. actual mASV forward velocity (in still water). The data points for each run are shown in black, the red dots indicate the mean values for each run, and the blue curve is a quadratic fitted to the mean data. The gray dashed line is the theoretical predicted relationship given by (4.2). (b) Flow sensor data from linear actuator with sensor mounted at various angles with respect to flow direction. Individual data points are shown as well as quadratic fits for each angle.	27
4.9 Linear actuator used to evaluate the flow sensors.....	28
4.10 The LoRe tank, showing (a) independently controlled motors and (b) bank of spinning cylinders.	29
4.11 (a) The HiRe tank and (b) a flow driving cylinder.	30
4.12 (a) Experimental setup of flow tank with 12 driven cylinders. (b) Flow field obtained via particle image velocimetry (PIV).....	31
4.13 MR tank and overhead motion capture camera system.	31
5.1 Trajectories of a team of 3 robots tracking the stable/unstable manifolds of the static double gyre system given by (2.4) with $A = 1$ and $s = 1$. The FTLE integration time is $T = 4$ sec.	34
5.2 Trajectories of a team of 3 robots tracking the coherent structures of the time-varying double gyre system given by (2.3). The FTLE integration time is $T = 4.5$ sec.....	34
5.3 Trajectories of teams of 3 robots performing tracking as in Section 5.2.2, but with increasing sensor noise intensities. In all frames, $t = 1.7$ and measurement noise is modeled as zero-mean Gaussian with $\sigma = \sqrt{2T}$. It can be seen that tracking fails with sufficiently high measurement noise.	36
5.4 Snapshots of the positions of agents at various times while tracking manifolds of the vector field given by (5.3). The top row (a)-(d) shows the team tracking the boundary, and the zoomed-in images in the bottom row (e)-(h) show the positions of the agents at the same times as (a)-(d) with the communication graph of the team overlaid. Leader agents are shown in red, while follower agents are shown in blue. The solid black line is the boundary being tracked.....	37
5.5 Trajectories of a team of 3 leader agents and 5 follower agents tracking the coherent structures of the time-varying double gyre system given by (2.3). The FTLE integration time is $T = 4.5$ sec.....	38
5.6 Trajectories of 3 simulated robots tracking a coherent structure using data obtained from the experimental testbed. In this simulation, the average velocity of the robots is slightly higher than the mean velocity of the underlying flow. To give a sense of time scale, tracer particles take roughly 10 seconds to recirculate through the gyres.	38
5.7 Approximate positions of the tank cylinders, and their rotational directions, in relation to the computed FTLE field.	38
5.8 Three simulated robots tracking a Lagrangian Coherent Structure off the coast of California over a 28 hour window.	39

6.1	(a) Photograph of the MR tank with a sample 3×3 static double gyre vector field overlaid and (b) photograph of three mASVs in the MR tank. Visible in (b) are the unique patterns of retro-reflective markers for overhead motion capture tracking.....	42
6.2	(a) Time invariant double gyre flow field with FLTE field overlaid and (b) paths of a 3 mASVs in MR tank tracking LCS in a simulated time invariant double gyre flow with FTLE field overlaid.....	42
6.3	Paths of 3 mASVs in the MR tank tracking a time varying LCS of a simulated double gyre flow given by (2.3).	43
6.4	Paths of 3 mASVs in the MR tank tracking a time varying LCS of a simulated double gyre flow given by (2.3) for two different experimental runs. Run (a) was performed without simulated sensor noise, while run (b) was performed with simulated sensor noise. The additive sensor noise was modeled as a zero-mean normal distribution with a standard deviation of 0.14 m/s.	44
6.5	Paths of 3 mASVs in the MR tank tracking a time varying LCS from actual flow data obtained in the High Reynolds number (HiRe) tank.....	44
6.6	Paths of 4 mASVs in the MR tank tracking manifolds of a simulated double gyre flow given by (2.4).	45
6.7	(a) Four spinning cylinders in the MR tank used to create a gyre like flow (overlaid) and (b) the paths of two mASVF _s moving through the flow while sampling the local flow velocity with onboard sensors. The trajectories of the mASVF _s are shown as dashed red curves and the flow measurements are shown as blue arrows. In both figures, the intended underlying flow field is shown in gray.....	46

Abstract

Tracking of Manifolds and Coherent Structures in Flows:
Simulations and Experiments

Matt Michini

Advisor: M. Ani Hsieh, Ph.D.

There has been a significant recent interest in using autonomous vehicles to study phenomena in the ocean including temperature and salinity profiles, contaminant transport, and biological processes such as plankton assemblages and algae blooms. It is challenging to deploy mobile robots with bounded actuation and limited communication in a highly nonlinear, time varying, and stochastic flow field such as the ocean. Despite natural stochasticity and arbitrary time dependence, geophysical flows do admit persistent transport controlling features known as Lagrangian coherent structures. These structures, which behave similarly to stable and unstable manifolds in time invariant dynamical systems, serve to characterize transport phenomena and have been shown to have many useful properties for ocean sampling and efficient navigation.

In this work, a strategy for tracking manifolds of 2D conservative vector fields is described and the application of this strategy to track coherent structures in general time dependent flows is presented. Computer simulations of the tracking strategy on a variety of analytical and measured flow fields are presented, and it is shown that, in many cases, the strategy is capable of successfully tracking coherent structures in simulation. In addition, the development of an experimental testbed consisting of a fleet of small autonomous surface vessels and three flow tanks is described. Preliminary experimental results related to tracking coherent structures using this flow testbed are presented. The overall results of this effort have indicated that the tracking strategy, although designed for time invariant flows, can be used to track coherent structures in certain time dependent flows quite reliably.

1. Introduction

1.1 Motivation

There is a recent interest in using autonomous vehicles as mobile sensors to study phenomena in geophysical flows such as the ocean. Autonomous ocean-going vehicles include autonomous surface vehicles (ASVs) and autonomous underwater vehicles (AUVs), and they are useful in the sense that, unlike stationary sensors, they can be actively deployed in nearly any spatial arrangement and can cover large regions of a flow field. Operation of ASVs and AUVs in the ocean presents many challenges, including the need to operate vehicles with potentially limited actuation in highly stochastic, strongly time varying flows.

Such flows have been shown to exhibit patterns which strongly govern transport properties such as tracer particle trajectories. These patterns are generically referred to as coherent structures [33]. When these structures are defined using some metric obtained from trajectories in the flow, they are referred to as Lagrangian coherent structures (LCS). Because of their transport-controlling properties, these structures behave similarly to separatrices which divide the phase space (or, equivalently, fluid flow) into dynamically distinct regions. A simple example of an LCS is a stable manifold of a hyperbolic equilibrium point in a time invariant flow.

In two dimensions, the presence of an LCS is in some cases indicated by a one-dimensional ridge of high values in the finite-time Lyapunov exponent field.¹ The finite-time Lyapunov exponent (FTLE) is related to the classic Lyapunov exponent in dynamical systems which provides a measure of divergence of infinitesimally close trajectories (and thus a measure of chaos), except that the FTLE is computed over a finite time horizon. The FTLE field provides a measure of the rate of divergence of initially *nearby* trajectories, and thus provides a picture of the behavior of the flow in a Lagrangian sense. LCS are useful for studying flows with arbitrary time dependence, especially because they characterize transport but also because they have been shown to correspond to time and fuel optimal glider paths in the ocean. These structures are also useful for defining boundaries of stochastic eddies, and have been shown to be useful for predicting contaminant transport in the ocean. In addition, LCS have been shown to correspond to regions of a flow where mobile sensors tend to escape their monitoring region of interest [6].

¹In an arbitrary dimension, LCS are codimension-1 manifolds as long as certain conditions are met (i.e., areas not in expansion or compression)

For the reasons enumerated above, it is evident that a map of the locations of coherent structures in a region of the ocean would prove tremendously useful. Such a map, however, is impossible to construct in real time unless the flow field is either time invariant, periodic, or can be predicted to a specified horizon. This is because LCS are inherently *Lagrangian* constructs, meaning their definition is based on the future evolution of the flow, unlike instantaneous strain metrics such as the Okubo-Weiss criterion [33]. Currently, the only way to construct a map of LCS for a flow field with arbitrary time dependence is to obtain velocity data over a specified period of time then compute the FTLE field, resulting in a map of the coherent structures in a flow at a previous time; i.e., delayed by a time T (the FTLE integration time).

It is of great interest to be able to track the locations of LCS in real time using solely local flow measurements. Since LCS are analogous to stable and unstable manifolds in time invariant dynamical systems, this is similar to the problem of tracing out stable trajectories in a time invariant system. The proper interior maximum (PIM) triple method [25] provides a numerical technique intended to find trajectories in a chaotic dynamical system which remain in a region with no attractors for an arbitrarily long period of time. This is analogous to the problem of finding stable manifolds of hyperbolic equilibrium points (saddle points) in time invariant dynamical systems. The PIM triple technique accomplishes its goal by iteratively tracing out stationary trajectories in such regions using ‘measurements’ of the phase space which lie only along a line segment. It therefore only requires local knowledge of the underlying flow field. This technique has been extended to the case whereby only three measurements of the flow field (taken, for example, by mobile sensing robots) are available along the line segment [16]. These measurements can be interpolated along the line segment and a minimum interpolated velocity reliably indicates the location of a stable trajectory in 2D conservative flows.

This work presents a manifold tracking strategy for three robots which is guaranteed to be able to trace out stable and unstable manifolds in time invariant, 2D conservative vector fields. The extension of this technique to tracing coherent structures in time varying flows is presented, and is evaluated using both computer simulations and laboratory experiments. In addition, an attempt to add robustness to the tracking strategy by adding more sensing agents is presented. Results from this work indicate promise for using such a strategy in actual ocean environments. In essence, this work seeks to provide first steps and a proof-of-concept toward actual deployment of sensing robots into flows for real-time LCS tracking.

1.2 Related Work

The concept of coherent structures in general time dependent flows has existed for some time in the fluid mechanics literature, but a series of papers by Haller et al. sought to precisely define the notion of Lagrangian coherent structures [8–11], and a more formal definition is given by Shadden et al. [33] More recent work by Haller sought to further study the relationship between strain field invariants and LCS [12, 13, 30]. Many applications of LCS have been discussed in the literature. Several works have hypothesized the use of LCS for predicting contaminant transport [19, 26], and knowledge of LCS locations has been shown to aid in efficient navigation in the ocean [17, 32, 40]. Using LCS to improve mobile sensor deployment in the ocean has also been discussed [6, 20].

The PIM triple method was first proposed by Nusse [25], and the collaborative manifold tracking strategy based on the PIM triple method was proposed by Hsieh et al. [16]. Many works address the problem of multi-robot collaborative boundary tracking (e.g., [7, 15, 36, 37]).

The work presented in this thesis is distinct from the above in that it addresses the problem of real-time tracking of LCS in general time-varying flows. Many of the works related to useful applications of LCS require a priori knowledge of the locations of LCS curves, which is not an explicit requirement of this work.

1.3 Contributions of this Thesis

The manifold and coherent structure tracking strategy presented herein has previously been shown to have significant promise based on initial results [16]. This work seeks to provide a next step by more rigorously evaluating the strategy in a broader sense; that is, with a wider variety of flow environments and mobile robots. Based on the results presented in this work, a discussion as to the possibility of extending the manifold and coherent structure tracking strategy to larger scale testing and actual deployments of mobile robots into geophysical flow environments is better informed.

Much of what is presented in this thesis is based on previously published work [18, 21–24]. The central contributions of this thesis are:

1. The implementation of the proposed manifold and coherent structure tracking strategy in computer simulations using data from a variety of sources, including simple analytical vector fields, measured flows from laboratory scale flow tanks, and measured ocean currents.

2. The design and development of a testbed for experimentally evaluating the proposed tracking strategy. Particularly, the development of a novel class of small autonomous surface vessels (ASVs) for deployment into a laboratory scale flow tank.
3. The experimental implementation of the proposed strategy using the ASVs and the laboratory scale flow testbed, and the experimental evaluation of the flow sensing capabilities of the ASVs.
4. Based on these results, an evaluation and discussion of the strengths and limitations of this strategy and its feasibility for tracking Lagrangian coherent structures in an ocean environment.

This thesis presents a detailed exposition and discussion of these contributions.

1.4 Overview

This thesis is organized as follows. Chapter 2 presents an overview of relevant background information, including the mobile robot kinematics model used as a basis for the tracking strategy as well as the various fluid flow models used throughout the work. Chapter 2 also formally introduces two concepts of great importance to this work; namely, the finite-time Lyapunov exponent (FTLE) and Lagrangian coherent structures (LCS). The manifold and coherent structure tracking strategy that forms the basis of this work is summarized in Chapter 3.

Results presented in this thesis are broadly divided into simulations and experiments. First, a detailed description of the experimental testbed, which comprises several flow tanks and a fleet of mobile robots, is provided in Chapter 4. Simulation results and an overview of simulation methods used are presented in Chapter 5, and experimental methodologies and results are presented in Chapter 6. Finally, a summary of this work, including potential directions for future work, is presented in Chapter 7.

2. Background

This chapter first presents a kinematics model of the 2D mobile robots used in both simulations and experimental validation of the manifold and coherent structure tracking strategy. The tracking strategy is evaluated with a variety of analytical vector fields, experimentally measured flows, and measured ocean flows; these flow models are detailed in Sections 2.2 and 2.3. In Section 2.4, the concept of the finite-time Lyapunov exponent (FTLE) is defined, and numerical computation of FTLE fields for both analytical models and discrete flow data is described. Finally, Lagrangian coherent structures (LCS), which are related to FTLE fields, are defined and exemplified in Section 2.5.

2.1 Kinematics Model

Each mobile robot is assumed to be 2D nonholonomic vehicle with differential drive actuation. Then the kinematics for vehicle i is given by

$$\dot{x}_i = V_i \cos \theta_i + u_i, \quad (2.1a)$$

$$\dot{y}_i = V_i \sin \theta_i + v_i, \quad (2.1b)$$

where $\mathbf{x}_i = [x_i, y_i]$ denotes the position of the i^{th} vehicle in the global coordinate frame, V_i denotes the forward velocity of the vehicle with respect to the flow, and θ_i represents the vehicle's heading (i.e., the angle made between the vehicle's forward direction and the x -axis of the global frame). The term $\mathbf{u}_i = [u_i, v_i]$ denotes the velocity of the flow field (represented in the global frame) at \mathbf{x}_i . This model is analogous to the common unicycle kinematics model, except that the no-sideslip constraints are made with respect to the flow field instead of the global coordinate frame, which ensures that the robots do not experience any velocity perpendicular to their direction of travel relative to the flow.

In this work, it is assumed that the flow velocities \mathbf{u}_i in (2.1) are given by 2D vector fields of the form

$$\dot{\mathbf{x}} = \mathbf{F}(\mathbf{x}), \quad (2.2)$$

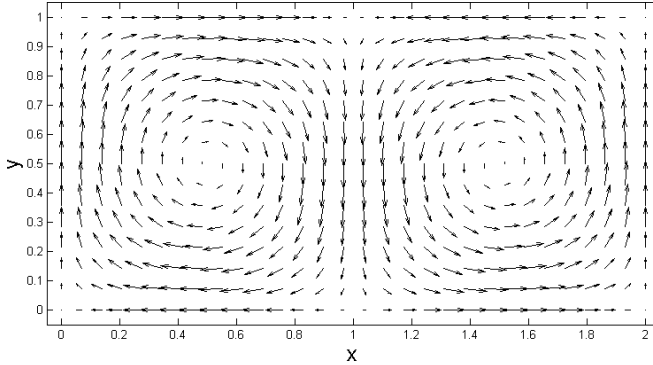


Figure 2.1: Phase portrait for the model given by (2.3) with $A = 1$, $\mu = 0$, $\varepsilon = 0$, $\psi = 0$, and $s = 1$.

where $\mathbf{x} \in \mathbb{R}^2$ and $\mathbf{F} : \mathbb{R}^2 \mapsto \mathbb{R}^2$. This means that the velocity of the flow field at vehicle i 's location is given by $u_i = F_x(\mathbf{x}_i)$ and $v_i = F_y(\mathbf{x}_i)$. Note that for a conservative flow field, $\mathbf{F}(\mathbf{x}) = \nabla f(\mathbf{x})$, where $f(\mathbf{x})$ is a scalar potential function and ∇ is the gradient operator. For the theoretical development of the tracking strategy, the flow field is assumed to be time-invariant and conservative. However, the strategy is evaluated and tested on both time-invariant and time-varying flows. The flow models used to evaluate the tracking strategy are detailed in Sections 2.2 and 2.3.

2.2 Flow Models

The wind-driven double gyre model provides a useful framework for evaluating the multi-robot LCS tracking strategy and is given by

$$\dot{x} = -\pi A \sin\left(\pi \frac{f(x, t)}{s}\right) \cos\left(\pi \frac{y}{s}\right) - \mu x, \quad (2.3a)$$

$$\dot{y} = \pi A \cos\left(\pi \frac{f(x, t)}{s}\right) \sin\left(\pi \frac{y}{s}\right) \frac{df}{dx} - \mu y, \quad (2.3b)$$

$$f(x, t) = \varepsilon \sin(\omega t + \psi) x^2 + (1 - 2\varepsilon \sin(\omega t + \psi)) x. \quad (2.3c)$$

When $\varepsilon = 0$, the double-gyre flow is time-independent, while for $\varepsilon \neq 0$, the gyres undergo a periodic expansion and contraction in the x direction. In (2.3), A approximately determines the amplitude of the velocity vectors, $\omega/2\pi$ gives the oscillation frequency, ε determines the amplitude of the left-right motion of the separatrix between the gyres, ψ is the phase, μ determines the dissipation, and s scales the dimensions of the workspace.

Figure 2.1 shows the phase portrait of the double-gyre model for $\varepsilon = \mu = 0$. Some of the useful properties of this model can be seen in the figure. For example, it can be seen that the flow is clearly

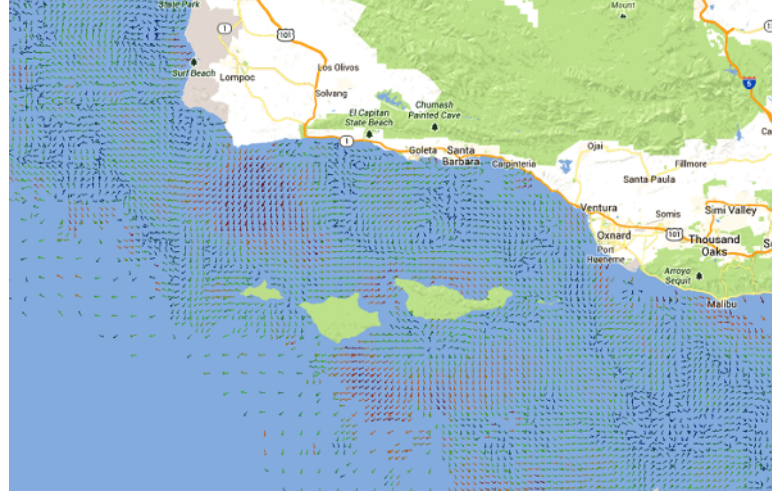


Figure 2.2: Sample high-frequency (HF) radar derived hourly coastal ocean current data from the Southern California Coastal Ocean Observing System.

divided into dynamically distinct regions, and nearby trajectories originating on opposite sides of the separating boundaries diverge very quickly from each other. This property is explained and quantified in Sections 2.4 and 2.5.

Because of their useful properties, both the time invariant and time varying versions of (2.3) are used extensively in this work to evaluate the LCS tracking strategy under various circumstances. When the model is time invariant, it is referred to as the *static* double gyre. In this case, the dissipation μ is often set to zero and the model is given by

$$\dot{x} = -\pi A \sin\left(\frac{\pi x}{s}\right) \cos\left(\frac{\pi y}{s}\right), \quad (2.4a)$$

$$\dot{y} = \pi A \cos\left(\frac{\pi x}{s}\right) \sin\left(\frac{\pi y}{s}\right). \quad (2.4b)$$

2.3 Ocean Model

The coherent structure tracking strategy described in this work is ultimately intended to be used to track flow features in actual ocean environments using teams of ocean-going autonomous vehicles. It is therefore important to utilize actual flow data from the ocean for the validation of the tracking strategy.

The United States coast is instrumented with a system of many high-frequency (HF) radar stations capable of resolving surface currents at various spatial and temporal resolutions. Real-time and historical data is available from the Southern California Coastal Ocean Observing System

hosted by the Scripps Institution of Oceanography at the University of California, San Diego [2]. A snapshot of this data for the California Coast is shown in Figure 2.2. The data presented in the figure is updated hourly, and both 2 km and 6 km spatial resolutions can be seen. This data is used to evaluated the tracking strategy, as detailed in Section 5.5.

2.4 Finite-time Lyapunov Exponents (FTLE)

In dynamical systems theory, the standard Lyapunov exponent is used to measure the rate of separation of infinitesimally close trajectories in the phase space of a dynamical system [35]. The Lyapunov exponent provides a useful tool for analyzing nonlinear time-varying dynamical systems, most notably because large positive values of Lyapunov exponent indicate chaos, which itself describes a sensitive dependence on initial conditions. If (2.5) describes the divergence of two trajectories with initial (very small) separation δ_0 , then λ is called the Lyapunov exponent.

$$|\delta(t)| \approx |\delta_0|e^{\lambda t} \quad (2.5)$$

The Lyapunov exponent is typically computed by taking an infinite limit or integral; unfortunately, most experimental and measured flow data is bounded in space and time. A suitable approximation of the Lyapunov exponent for such cases is called the finite-time Lyapunov exponent (FTLE), which compares divergence of nearby trajectories after a fixed amount of time [5]. The FTLE is distinct from the well-known Okubo-Weiss criterion in that it is not an instantaneous measure of separation. Rather, trajectories are integrated over a specified length of time, resulting in a metric more revealing of the actual transport properties of the flow [33]. By computing FTLEs over an entire vector field, a scalar field describing convergence/divergence of initially close trajectories is obtained.

In brief, the FTLE field is numerically computed by discretizing the domain into a regular grid and computing trajectories originating at each point in the grid. The trajectories are typically computed by numerically integrating the vector field (using a Runge-Kutta method, for example) over a fixed time period T . Separation of neighboring trajectories is quantified using a strain metric, resulting in a scalar FTLE value for each point.

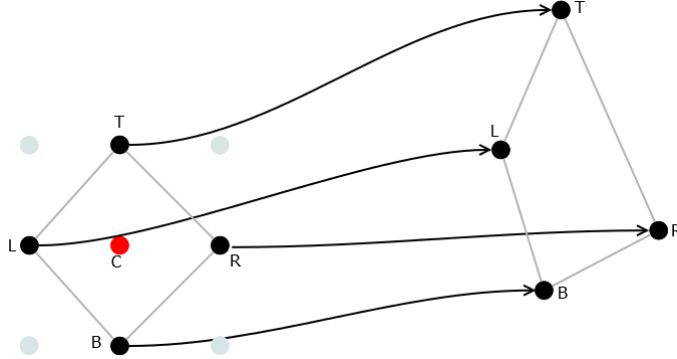


Figure 2.3: Diagram illustrating the initial and final locations of 4 advected particles in a flow.

2.4.1 Computation of the FTLE

To begin the FTLE computation, an initial grid of particles is defined. The spatial extent and number of particles of this grid affects the ‘resolution’ of the computed FTLE field. Using more particles, though more computationally costly, results in a finer representation of the field and may reveal features at smaller spatial scales. The particle trajectories from time t_0 to t_0+T are computed using a numerical integration method such as a Runge-Kutta adaptive method (implemented in Matlab as the `ode45` function), as illustrated in Figure 2.3.

Consider, without a loss of generality, the 2D case. Define the position of a sample particle on the grid to be x_C , and the positions of its immediate neighbors x_L , x_T , x_R , and x_B . The subscripts L , T , R , and B denote the left, top, right, and bottom neighbors, respectively. After trajectories are computed for each particle, a central difference approximation to the deformation gradient tensor \mathbf{G} is computed to quantify divergence of the trajectories:

$$\mathbf{G} = \begin{bmatrix} \frac{x_R(t_0+T)-x_L(t_0+T)}{x_R(t_0)-x_L(t_0)} & \frac{x_T(t_0+T)-x_B(t_0+T)}{y_T(t_0)-y_B(t_0)} \\ \frac{y_R(t_0+T)-y_L(t_0+T)}{x_R(t_0)-x_L(t_0)} & \frac{y_T(t_0+T)-y_B(t_0+T)}{y_T(t_0)-y_B(t_0)} \end{bmatrix}. \quad (2.6)$$

Now, let

$$\lambda = \max(\text{eig}(\mathbf{G}^T \mathbf{G})). \quad (2.7)$$

Since the field being defined is a *scalar* field, there is no need to be concerned about direction. Therefore, only the maximum eigenvalue of $\mathbf{G}^T \mathbf{G}$, which is representative of the largest deformation, is considered. The standard Lyapunov exponent equation is then applied to arrive at the value of

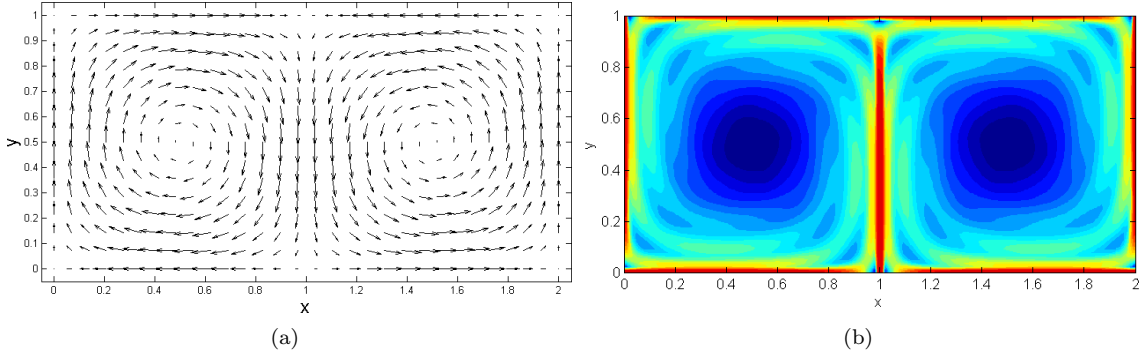


Figure 2.4: (a) Static double gyre vector field and (b) corresponding FTLE field for (2.4) with $A = 1$ and $s = 1$.

the FTLE for the particle x_C at time t_0 , which is given by

$$\sigma_{x_C}(t_0) = \frac{1}{|T|} \ln \sqrt{\lambda}. \quad (2.8)$$

The natural logarithm ensures that the metric describes *exponential* separation of nearby trajectories. Note that (2.8) is the value of the FTLE for only the particle x_C at time t_0 . The process outlined above is repeated for each particle in the grid to obtain an *FTLE field*. Note that for a general time-varying vector field, the FTLE field will vary with time as well. Therefore it is necessary to re-compute the entire FTLE field at various times in order to obtain a time-varying picture of the evolution of the flow.

The FTLE field can be readily visualized using a heat map or filled contour plot. As an example, consider the static double gyre vector field equations given by (2.4). This vector field and the corresponding FTLE field is shown in Figure 2.4. In the figure, red hues indicate higher FTLE values and blue hues indicate lower FTLE values. Very high FTLE values can be observed along the separatrix between the two gyres. This is because trajectories initially on opposite sides of the boundary diverge rapidly from each other. To emphasize a previous point, since this vector field is time-invariant, the FTLE field is time-invariant as well. However, for the time-varying double gyre model given by (2.3), the FTLE field is also time-varying.

2.4.2 Computation of FTLE Field using Discrete Flow Velocity Data

It is often the case that the FTLE field must be computed for a region for which flow data is available only at specified locations and times. Usually, this data is arranged in a regular grid in $n+1$

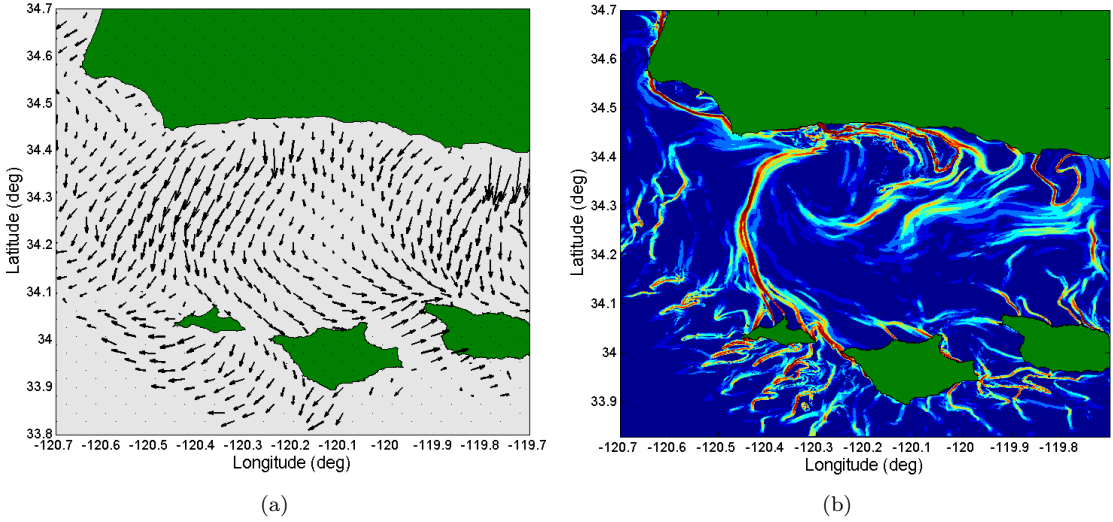


Figure 2.5: (a) Sample HF radar derived ocean current data for the Santa Barbara Channel and (b) corresponding FTLE field, computed with an integration time of 24 hours.

dimensional space, where n is the spatial dimension and time accounts for the extra dimension. In this case, the raw data must be interpolated so that accurate particle trajectories may be computed using numerical integration.

For 2D data, the x and y velocity components are treated as scalar fields and interpolated separately. For each component, a trilinear interpolation scheme over the two spatial dimensions and the time dimension is employed. Note that the decision to interpolate using the x and y velocity components is arbitrary; in fact, vector field interpolation in general is non-unique [31]. Also, while more advanced multivariate interpolation schemes are available (e.g., tricubic), it has been found that the trilinear scheme results in sufficiently smooth data for simulating coherent structure tracking and for computing FTLE fields. Indeed, it has been found that FTLE maxima are relatively insensitive to the interpolation scheme used for the computation [14]. Once an interpolant is fitted to the raw data, the computation can proceed as described in the previous section. Figure 2.5 illustrates an example of an FTLE field computed using measured ocean currents.

Computing FTLE fields using experimental data is made difficult by the fact that the data is spatially bounded and may contain regions for which there is no valid data (this can occur in ocean data, for example, when a particle reaches land). Particle trajectories are typically computed over relatively long periods of time; therefore it is common for a particle to exit the domain of available data before the specified integration time T . In this case, computation of the particle trajectory

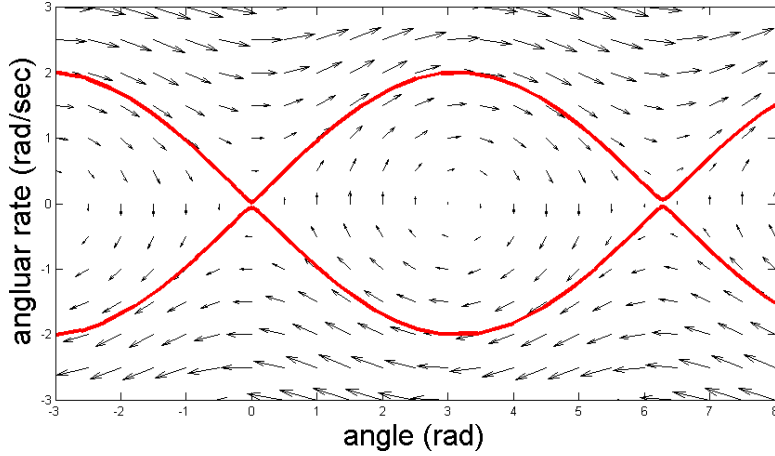


Figure 2.6: Phase portrait of a simple pendulum.

must cease and FTLE values for the particle's neighbors must be computed at that time. This effectively limits the integration time window T for actual flows, as the FTLE fields begin to betray the actual behavior of the flow when too many particles prematurely exit the domain.

2.5 Lagrangian Coherent Structures (LCS)

In time-invariant dynamical systems, stable and unstable manifolds of a saddle point divide the phase space into dynamically distinct regions. Consider, for example, the phase portrait of a simple pendulum, as shown in Figure 2.6. The stable and unstable manifolds, highlighted in red, divide the flow into distinct regions. That is, the region enclosed by the manifolds (in the center of the image) contains trajectories for which the pendulum oscillates back and forth (repeatedly changing directions of rotation). The regions above and below the manifolds contain trajectories for which the pendulum continuously rotates in the same direction. These two dynamical behaviors are qualitatively quite distinct, and the stable and unstable manifolds form clear boundaries for them in the phase space.

This notion of stable and unstable manifolds is well-defined for time-invariant systems, but there is no direct analogue for systems with arbitrary time dependence. However, by examining the behavior of particle trajectories over time, it is possible to define an analogous concept for time varying flows. Because it deals with particle trajectories, the FTLE field, as described above, carries information about the evolution of the flow in a Lagrangian sense.

In particular, ridges of high FTLE values indicate manifolds for which nearby trajectories diverge

over time. These ridges have been shown to indicate the presence of Lagrangian coherent structures, and evidently they divide the flow into dynamically distinct regions similarly to stable and unstable manifolds in time-invariant systems. As an example, consider the FTLE field pictured in Figure 2.5. The curve of high FTLE values (indicate by red hues) stringing from the mainland to the leftmost island is an LCS.

There are some compelling reasons to study these structures. First, LCS act as transport barriers. As an example, consider an isolated mass of surface ocean water entrained in an eddy. Eddies have been observed to travel long distances and transport nutrients that can trigger biological productivity in otherwise depleted regions of the ocean. The boundaries of these eddies are traditionally hard to find using only velocity data, but they are easily revealed by computing the FTLE field. Similarly, knowledge of LCS can aid in predicting contaminant transport such as an oil spill. Tracking the locations of LCS near a mass of oil on the ocean surface may allow better prediction of its transport and better allocation of resources [26].

Beyond just characterizing transport, LCS can be useful from a path planning perspective, in that they have been shown to correspond to time and fuel optimal glider paths in the coastal ocean [17]. This result suggests that if autonomous vehicles can find and track these structures, they can leverage the dynamics of the flow for efficient navigation, instead of only treating the dynamics as a disturbance.

2.6 Summary

This chapter presented a simple kinematics model used for each of the mobile robots in this work. This simple unicycle-like model treats velocity with respect to the flow and heading as control inputs, and describes the effect of the vector field \mathbf{F} on the motion of the robots. Several analytical flow models and the ocean model used to evaluate the coherent structure tracking strategy in simulation were presented. In addition, the concept of the finite time Lyapunov exponent (FTLE) was formalized and the numerical computation of FTLE fields was described. Lagrangian coherent structures were introduced, and it was shown that ridges of high values in the FTLE field sometimes correspond to LCS. Also, some interesting properties of LCS were discussed.

3. Manifold and Coherent Structure Tracking Strategies

In Chapter 2, the notion of Lagrangian coherent structures was defined and some of their interesting properties were described. It was noted that knowledge of the locations of LCS in real time is useful for many aspects of ocean study, including predicting transport and finding fuel and time efficient paths. Mobile sensing robots provide an ideal platform for performing such a tracking task, since they can be deployed in any number of arrangements. Unlike fixed sensors, a team of robots can be reconfigured to match relevant spatial and temporal scales of a given flow, allowing greater flexibility.

It is thus desired to employ a team of mobile robots to track the locations of coherent structures in real time. Since LCS are extensions of stable and unstable manifolds in time-invariant systems, the development of the control strategy begins by assuming a time-invariant, conservative vector field. Although real geophysical flows are in general neither conservative nor time-invariant, this assumption eases analysis and simplifies implementation, such that certain guarantees of the success of the strategy can be made in this limited sense. The strategy is subsequently applied to flows which disobey these assumptions but nonetheless exhibit similar features.

3.1 Three Robot LCS Tracking Strategy

Consider the problem of controlling a group of three 2D vehicles to collaboratively track coherent structures, which are 1D curves that separate regions of the flow with distinct dynamical behavior. As mentioned above, this is similar to the problem of tracking stable (and unstable) manifolds of a general nonlinear dynamical system. Assume the 2D kinematic model given by (2.1) for each of the vehicles, where V_i and θ_i are taken to be control inputs. For the theoretical development of the tracking strategy, it is assumed that $\mathbf{u}_i = [u_i, v_i]$ in (2.1) is provided by a 2D planar conservative vector field.

Let B_S and B_U denote the stable and unstable manifolds of (2.2). In general, B_S and B_U are the separating boundaries between regions in phase space with distinct dynamics. For 2D flows, B_* are simply one-dimensional curves where $*$ denotes either stable (S) or unstable (U) boundaries. For a small region centered about a point on B_* , the system is unstable in one dimension. Finally, let $\rho(B_*)$ denote the radius of curvature of B_* and assume that the minimum of the radius of curvature

$\rho_{min}(B_*) > d_{Max}$ where d_{Max} is a positive constant. This requirement ensures that the robots do not lose track of B_* because the boundary has too many sharp turns.

The methodology is inspired by the Proper Interior Maximum (PIM) Triple Procedure [25], which is an iterative numerical technique designed to find stationary trajectories in chaotic regions with no attractors. While the original procedure was developed for chaotic dynamical systems, the approach can be employed to reveal the stable set of a hyperbolic fixed point of a general nonlinear time invariant dynamical system. Note that while the focus is on the development of a tracking strategy for the stable manifolds B_S , the technique can be easily extended to track B_U , since B_U are simply stable manifolds of (2.2) for $t < 0$.

The procedure consists of iteratively finding an appropriate PIM Triple on a saddle straddling line segment and propagating the triple forward in time. Let the initial positions of the three leader agents be denoted $\{\mathbf{x}_L(t_0), \mathbf{x}_C(t_0), \mathbf{x}_R(t_0)\}$ and assume that they are initially configured in a valid saddle-straddling formation J_{t_0} , i.e., agents L and R begin on opposite sides of B_s . Different from the original PIM triple procedure, only local velocity measurements are used to estimate the location of the next PIM triple line segment.

Let $d(\cdot, \cdot)$ denote the Euclidean distance function and assume that $d(\mathbf{x}_C, B_S) < \epsilon$ such that $\epsilon > 0$ is small. Then given the straddle line segment J_{t_0} such that $\mathbf{x}_L(t_0)$ and $\mathbf{x}_R(t_0)$ are the endpoints of J_{t_0} , consider an $\epsilon_t < \epsilon$ discretization of J_{t_0} such that $\mathbf{x}_L = \mathbf{q}_1 < \mathbf{q}_2 < \dots < \mathbf{q}_M = \mathbf{x}_R$. Since agents can only measure flow velocities at their respective locations, the Inverse Distance Weighting method [4] is used to estimate the flow velocities at points $\mathbf{q}_1, \dots, \mathbf{q}_M$. For a given set of velocity measurements $\mathbf{u}_i(t)$ and corresponding positions $\mathbf{x}_i(t)$, the velocity vector at some point \mathbf{q}_k is given by

$$\mathbf{u}(\mathbf{q}_k) = \sum_j \sum_{i=1}^N \frac{w_{ij} \mathbf{u}_i(j)}{\sum_j \sum_{i=1}^N w_{ij}}$$

where $w_{ij} = \|\mathbf{x}_i(j) - \mathbf{q}_i\|^{-2}$. While there are numerous vector field interpolation techniques available, the inverse distance weighting method is chosen due to its ease of implementation as well as its reliance on data that can be obtained via local sensing alone.

Then the estimate of the manifold location along J_{t_0} is given by $\mathbf{q}_B(t_0) = \mathbf{q}_j$ where $j = \arg \max_{k=1, \dots, M} (\mathbf{u}(\mathbf{q}_k))$. Then the midpoint of the *projected* saddle straddling line segment $J_{t_0+\Delta t}$ is computed as $\mathbf{q}_C(t_0 + \Delta T) = \mathbf{q}_B(t_0) + b\hat{\mathbf{u}}(\mathbf{q}_B(t_0))$, where $b \in \mathbb{R}^+$ is a constant gain chosen such that the projected line segment remains *ahead* of the team. The new saddle straddling line segment $J_{t_0+\Delta T}$

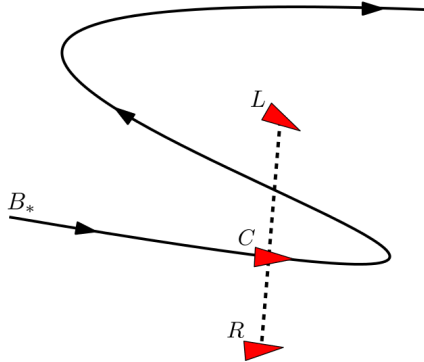


Figure 3.1: An errant case illustrating the need for $d_{Max} < \rho_{min}(B_*)$. Here, L and R , traversing from left to right, end up on the same side of the boundary and no longer form a valid saddle straddling line segment.

is constructed to be orthogonal to $\hat{\mathbf{u}}(\mathbf{q}_B(t_0))$ and thus nearly orthogonal to B_s . Finally, the control inputs of the L , C , and R agents are computed such that L and R move toward the endpoints of $J_{t_0+\Delta T}$ and C moves toward the midpoint of $J_{t_0+\Delta T}$. That is, the desired velocities \mathbf{V}_{d_i} (in the global frame) for agents L , C , and R are given by

$$\mathbf{V}_{d_i} = a(\mathbf{q}_i(t_0 + \Delta T) - \mathbf{x}_i(t_0)) \quad (3.1)$$

for $i = \{L, C, R\}$, where \mathbf{x}_i is the position of the i^{th} agent in the global frame, $\mathbf{q}_i(t_0 + \Delta T)$ is the respective midpoint or endpoint of the projected saddle-straddling line segment, and $a \in \mathbb{R}^+$ is a gain.

Note that since the team estimates the location of B_* by identifying the location along the saddle straddling line segment J_{t_0} where the maximum current occurs, robots L and R must maintain the saddle straddling formation to ensure the team does not lose track of the boundary. As such, d_{Max} must be chosen such that $\rho_{min}(B_*) > d_{Max}$. This is to ensure that sharp turns in B_* do not cause robots L and R to end up on the same side of the boundary/manifold. Figure 3.1 illustrates an errant case for which $d_{Max} > \rho_{min}(B_*)$. In the figure, L and R end up on the same side of the boundary and cease to maintain a saddle straddling line segment. Note that in realistic flows, $\rho_{min}(B_*)$ is difficult to estimate, and so a suitable d_{Max} must be selected.

This three-robot strategy has been shown to be able to maintain a valid saddle straddling formation across B_* , as long as the robots are initially arranged in a saddle straddling formation [16, 22].

3.2 LCS Tracking with Formation Control

Though the original manifold and coherent structure tracking strategy described in 3.1 is intended for three agents, adding additional sensing agents can improve the overall estimation of the underlying flow and improve robustness of tracking. The original three-agent strategy was thus extended to an N -agent leader-follower strategy. The result is a distributed formation control strategy that leverages the spatio-temporal capabilities of the team to track the stable/unstable manifolds of general 2D conservative flows using only local sensing and communication. The major advantage of using a larger team of autonomous vehicles is that the team can simultaneously cover larger physical regions and/or achieve finer spatio-temporal sampling of the flow field, resulting in better estimates of the underlying vector field.

Specifically, consider $N > 3$ agents, which includes 3 leader agents and $N - 3$ follower agents. All agents are assumed to be able to sample the local velocity field and broadcast their measurements to the leader agents, who adjust their motion based on the 3-agent tracking strategy described in Section 3.1. Different from the original strategy, though, the formulation presented in this section enables the leaders to maintain a triangular saddle straddling formation across B_* . Agents L and R actuate toward the endpoints of the projected boundary-straddling line segment $J_{t_0+\Delta T}$, similarly to the above strategy, such that the desired velocities \mathbf{V}_{d_i} (in the global frame) for agents L and R are given by (3.1). In this case, however, agent C attempts to maintain a triangle formation with respect to agents L and R . That is, the desired velocity of agent C (in the global frame) is given by:

$$\mathbf{V}_{d_C} = a(\mathbf{q}_C(t_0 + \Delta T) - d_{\perp} \hat{\mathbf{u}}(\mathbf{q}_B(t_0)) - \mathbf{x}_C(t_0)) \quad (3.2)$$

where \mathbf{x}_C is the position of agent C in the global frame, $\mathbf{q}_C(t_0 + \Delta T)$ is the midpoint of the projected saddle-straddling line segment (as above), $a \in \mathbb{R}^+$ is a gain, and $d_{\perp} \in \mathbb{R}$ is a parameter affecting the ‘height’ of the triangle formation, i.e., the desired perpendicular distance between agent C ’s location and the line segment connecting agents L and R . A diagram of the strategy is shown in Figure 3.2.

Note that desired velocities given by (3.1) and (3.2) can be decomposed into local velocity commands V_i and angles θ_i for $i = \{L, C, R\}$ using (2.1) so that:

$$V_i = \|\mathbf{V}_{d_i} - \mathbf{u}_i\| \quad (3.3a)$$

$$\theta_i = \text{atan2}((\mathbf{V}_{d_i} - \mathbf{u}_i)_y, (\mathbf{V}_{d_i} - \mathbf{u}_i)_x) \quad (3.3b)$$

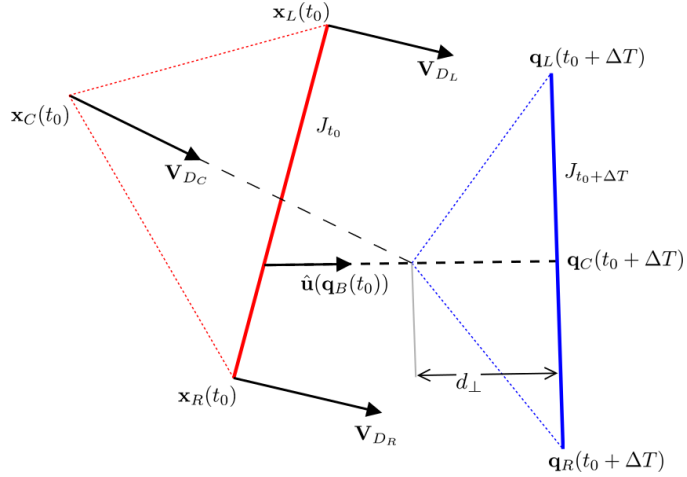


Figure 3.2: Diagram of the 3-agent tracking strategy. The current saddle-straddling line segment J_{t_0} is indicated by a solid red line, and the projected straddling line segment $J_{t_0 + \Delta T}$ is indicated by a solid blue line. The vertices of the red triangle are thus the current positions of the robots, and those of the blue triangle are the desired positions after time ΔT .

where \mathbf{u}_i is the flow velocity expressed in the global frame at \mathbf{x}_i and $\text{atan2}(y, x) : \mathbb{R}^2 \mapsto (-\pi, \pi]$ is the two-argument arctangent function.

With the leader agents' control inputs determined by the above tracking strategy, a formation control strategy is required for the additional sensing agents (viz. the follower agents) in the swarm. It is essential that the formation control strategy precludes inter-agent collisions and ensures that follower agents remain in a geometrically bounded region such that data collection is effective and leader agents can prescribe collision-free paths in the environment. The follower agents' control inputs are thus computed based on the formation control strategy described by Rastgoftar et al. [27–29], which uses homogeneous transformations and continuum mechanics concepts to prescribe follower motions that satisfy the above requirements.

3.3 Summary

This chapter presented a control strategy to enable a team of robots to track invariant manifolds in 2D conservative flows. Based on the PIM triple method, the strategy allows the team of robots to iteratively trace out material lines that separate regions of the flow with distinct dynamical behavior. An extension of this strategy to a team of more than three agents using a leader-follower approach was also described. The main advantage of this approach is the ability to use flow measurements from any number of follower agents to improve the overall estimation of the flow field.

4. Experimental Testbed

An experimental testbed was developed at the Scalable Autonomous Systems Laboratory in order to produce high resolution and realistic quasi-2D flow fields that can be used to evaluate the performance of the multi-robot manifold and coherent structure tracking strategies. The experimental setup comprises two classes of autonomous surface vehicles (ASVs, sometimes referred to simply as ‘boats’) and three experimental flow tanks. From smallest in size to largest, the tanks are namely the Low Reynolds number (LoRe) tank, the High Reynolds number (HiRe) tank, and the Multi-Robot (MR) tank. The ASVs are described in detail in Section 4.1, and the flow tanks are described in Section 4.2.

4.1 Autonomous Surface Vehicles (ASVs)

A fleet of small autonomous surface vehicles (ASVs), which are designed to operate in the MR tank, has been developed for this work. The ASVs used in this work can be divided into two distinct classes, enumerated below:

1. The first class of vehicle used in this work is termed mASV (Micro Autonomous Surface Vehicle). It is a small, differential thrust aquatic robot with a wireless radio for receiving instructions from a central controller.
2. The second class of vehicle is termed mASVF (Micro Autonomous Surface Vehicle - Flow sensing). This class is nearly functionally identical to the first except that the vehicles are larger and contain sensors to detect the local fluid flow.

Examples of the two classes of vehicles are picture in Figure 4.1, and their important properties are compared in Table 4.1.

4.1.1 Design of the Vehicles

The flat-bottom hulls were designed with the goals of maximizing stability while minimizing size, and they are 3D printed using the selective laser sintering (SLS) process. In order to achieve proper weight and balance characteristics of the vehicle, a fully mass accurate CAD model was created in Solidworks. A rendering of the CAD model for the mASV is shown in Figure 4.2(a). This CAD

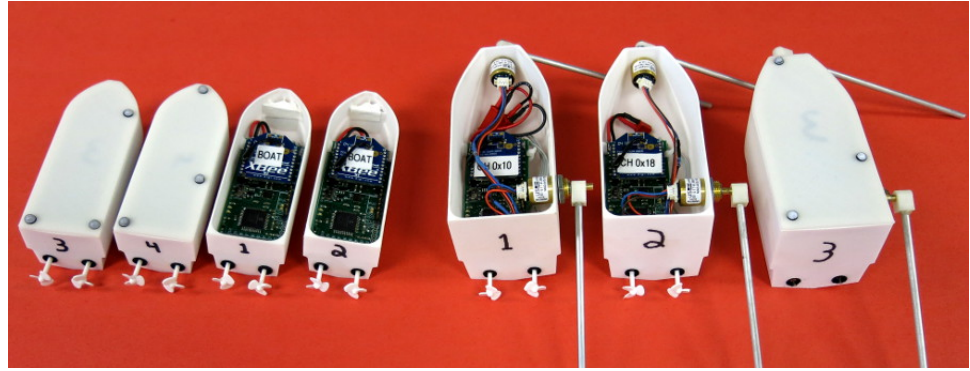


Figure 4.1: Examples of the two classes of autonomous surface vehicles used for this work, with and without 3D printed cap. Pictured on the left are the mASVs, and on the right are the mASVFs with flow sensors.

Table 4.1: Comparison of mASV and mASVF vehicle classes.

	mASV	mASVF
Mass	46.8 g	109.5 g
Moment of Inertia (yaw)	$3 \cdot 10^{-5} \text{ kg m}^2$	$1.2 \cdot 10^{-4} \text{ kg m}^2$
Overall length	10.2 cm	12.8 cm
Width	3.3 cm	6.3 cm
Draft	2.3 cm	3.2 cm
Max. forward speed	$\sim 0.2 \text{ m/s}$	$\sim 0.2 \text{ m/s}$
Max. turning rate	$\sim 2.0 \text{ rad/s}$	$\sim 1.0 \text{ rad/s}$
Forward drag coefficient	8.0 m^{-1}	unknown
Rotational drag coefficient	1.0 rad^{-1}	unknown
Battery life	$> 2 \text{ hours}$	$\sim 1 \text{ hour}$
Local flow measurement	none	2 flow sensing rod/encoder assemblies

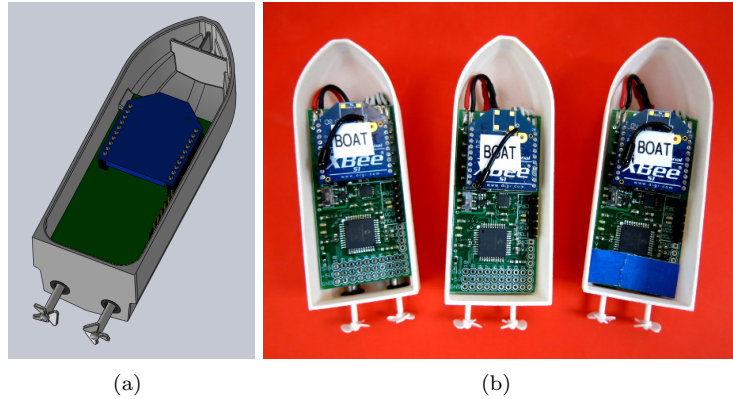


Figure 4.2: (a) 3D CAD model of an mASV and (b) photo of 3 mASVs.

model allows fine tuning of hull size and component placement to achieve the desired buoyancy characteristics. In addition, lead balls can be placed in small compartments at the front of the hull to trim the vehicle laterally and longitudinally.

Each mASV contains one 400 mAh lithium-polymer battery, while each mASVF contains two of these batteries connected in series, enabling a 5 V power source for the absolute encoders used for flow sensing. A pair of Faulhaber 0615 DC micro-motors power counter-rotating plastic propellers in a differential thrust configuration. A custom-built controller board provides power conditioning, communication, and motor control functionality. Communication is achieved using an XBee radio module, which acts as a wireless serial modem. A central control computer sends commands to each vehicle in a point-to-multipoint communication topology.

To reduce the chance of taking on water during maneuvers and high waves, each class of boat has a removable 3D-printed cap fitted with a silicone o-ring. In addition to providing protection from water infiltration, the caps are fitted with small (3 mm diameter) hemispherical retro-reflective markers. The adhesive-backed markers are arranged in a unique pattern for each vehicle, allowing the MR tank's OptiTrack motion capture system to distinguish among vehicles.

The components that make up the mASV and mASVF, along with their masses, are listed in Tables 4.2 and 4.3.

4.1.2 Custom Controller Board

The custom controller boards contain a PIC 8-bit microcontroller, a 6-axis accelerometer/angular rate sensor, and a pair of motor controller integrated circuits (ICs). The boards were laid out and

Table 4.2: Component list for the mASV vehicle class.

Component	Type	Qty	Unit Mass (g)	Total Mass (g)
Hull	Custom (3D printed)	1	11.5	11.5
Sealing Cap	Custom (3D printed)	1	6.6	6.6
Battery	Lithium Polymer (400 mAh)	1	9.3	9.3
Miniature DC Motor	Faulhaber 0615	2	2.0	4.0
4:1 Reducing Gearbox	Faulhaber 06/1	2	1.2	2.4
Sealing Rubber Grommet	McMaster P/N 9600K66	2	—	—
Propeller	Mini RC Boat	2	—	—
Controller Board	Custom	1	10.0	10.0
Radio Module	XBee Series 1 (1 mW)	1	3.0	3.0
Total mASV Mass				46.8

Table 4.3: Component list for the mASVF vehicle class.

Component	Type	Qty	Unit Mass (g)	Total Mass (g)
Hull	Custom (3D printed)	1	20.5	20.5
Sealing Cap	Custom (3D printed)	1	9.0	9.0
Battery	Lithium Polymer (400 mAh)	2	9.3	18.6
Miniature DC Motor	Faulhaber 0615	2	2.0	4.0
4:1 Reducing Gearbox	Faulhaber 06/1	2	1.2	2.4
Sealing Rubber Grommet	McMaster P/N 9600K66	2	—	—
Propeller	Mini RC Boat	2	—	—
Controller Board	Custom	1	10.0	10.0
Radio Module	XBee Series 1 (1 mW)	1	3.0	3.0
Encoder (flow sensor)	US Digital MA3	2	10.0	20.0
Flow Sensor Rod	Aluminum rod, $d = 3.2$ mm	2	3.0	6.0
Counterweight	Metal Standoffs	4	4.0	16.0
Total mASVF Mass				109.5

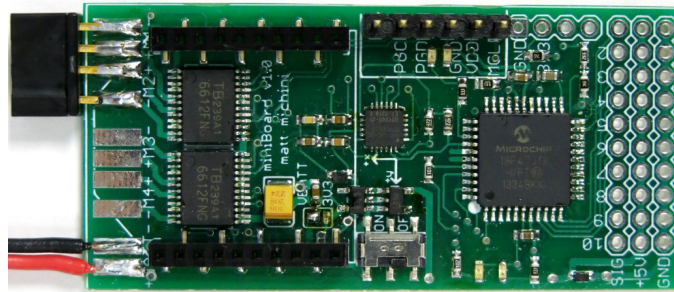


Figure 4.3: Custom controller board for the mASVs. Each board includes an 8-bit microcontroller, a 6-axis acceleration and angular rate sensor, and 2 motor controller ICs.

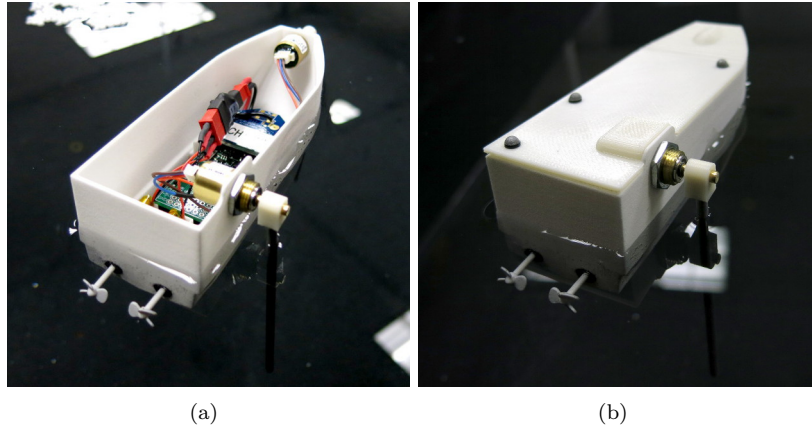


Figure 4.4: Inside view of the mASVF in the MR tank (a) without and (b) with unique pattern of retro-reflective markers.

routed using the Eagle software package, and the PCBs were fabricated by Advanced Circuits. Components were placed with solder paste and the boards were reflow soldered using a hot plate at the SAS lab. One of the custom boards is pictured in Figure 4.3.

4.1.3 Flow Sensor Design (mASVF)

The mASVF class vehicles are also equipped with onboard flow sensors. The size and mass constraints for the vehicles prohibit the use of more conventional external flow measurement devices, e.g., free-spinning propellers or acoustic sensors. Furthermore, most commercially available small lightweight flow sensors (e.g., hot-wire sensors) only measure flow *speed* and cannot be easily expanded or arranged to extract flow *velocity* given the size and mass constraints.

In light of this, the flow sensors are designed using a pair of lightweight and high resolution rotary encoders, each connected to an aluminum rod that extends into the water. Each aluminum rod is 120 mm in length and 0.32 mm in diameter and is affixed perpendicular to the shaft of the encoder. Figure 4.4 shows an mASVF in the MR tank, with one of the flow sensing rods visible. As the vehicle moves, drag experienced by the rod causes the angle measured by the encoder to vary; the angle of the encoder is then correlated to flow speed. By mounting the axes of rotation of the two rods orthogonal to each other, the full velocity vector of the flow field (referenced to vehicle's frame) is measured.

The angle of the encoder shaft is denoted ϕ and is given by:

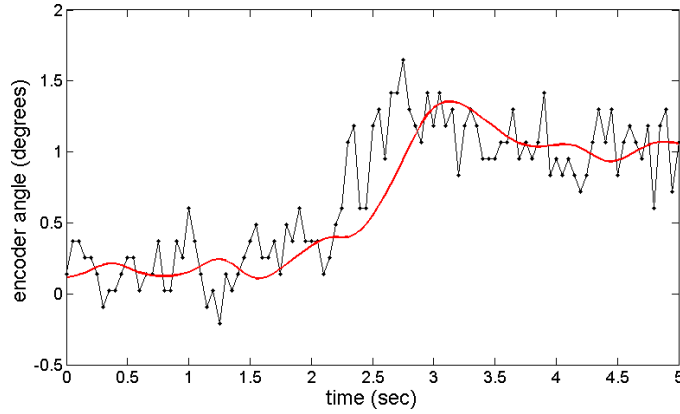


Figure 4.5: Unfiltered encoder angle data (black) and low-pass filtered data (red).

$$\phi = \frac{E_{enc}}{E_{cc}} 2\pi - \phi_{cal} \quad (4.1)$$

where E_{enc} is the output voltage of the encoder and is proportional to the angular displacement of the shaft, E_{cc} is the operating voltage of the controller board, and ϕ_{cal} is the baseline angle when the mASVF is at rest in still water. To mitigate quantization errors and noise, the encoder output is passed through a digital infinite impulse response (IIR) low-pass filter (a Type II Chebyshev filter was chosen for its low group delay property [34]). Figure 4.5 shows the unfiltered and filtered angular displacement data over a 5 sec window.

According to the free body diagram show in Figure 4.6, the theoretical relationship between the encoder angle ϕ and actual flow speed v is given by:

$$v = \sqrt{\frac{mgl_1 \sin \phi - F_B l_2 \sin \phi}{(l_2 \cos \phi)(\frac{1}{2}\rho C_D A_R)}} \quad (4.2)$$

where m is the mass of the rod, g is the acceleration due to gravity, l_1 is the distance from the pivot point to the center of mass of the rod, l_2 is distance from the pivot point to the center of mass of water displaced by the rod, F_B is the buoyant force due to water displaced by the rod, ρ is the density of water, C_D is the drag coefficient of the rod, and A_R is the frontal area of the rod in the water.

The objective is to estimate $\mathbf{u} = [u_i, v_i]^T$ using the two orthogonally mounted flow sensors onboard the vehicle and a vehicle's estimates for its inertial velocity $\dot{\mathbf{x}}$ and heading θ . In the MR tank, \mathbf{x} , $\dot{\mathbf{x}}$, and θ are provided via an external motion capture system. In the field, however, these

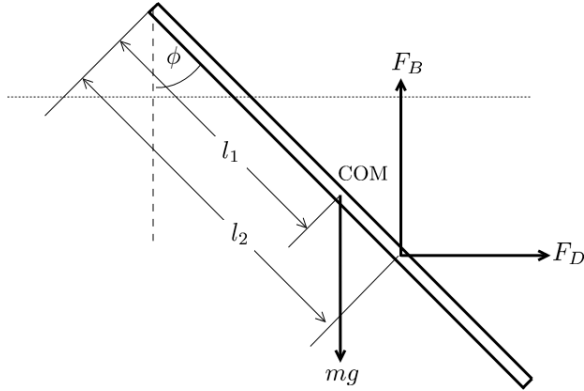


Figure 4.6: Free body diagram for the sensor rod, where the horizontal dashed line indicates water free surface level.

states can be estimated via deadreckoning, networks of underwater acoustic beacons [38, 39], GPS if the vehicles are surface vehicles, inertial sensors, or some combination of these.

The onboard flow sensor arrangement measures the vehicle's velocity relative to the flow, denoted by ${}^{ASV}\tilde{\mathbf{v}}$. To obtain the flow velocity at the mASV's position in the inertial frame, \mathbf{u} , the measured local velocity ${}^{ASV}\tilde{\mathbf{v}}$ must be mapped to the inertial frame. Let v_A and v_B represent the speeds obtained by flow sensors A and B , where sensor A measures speed in the direction of travel and B measures speed in the direction perpendicular to the direction of travel of the vehicle. Furthermore, let d_A and d_B represent the perpendicular distances from the center of mass of the vehicle to the respective flow sensor planes (see Figure 4.7(a)). Then the flow velocity measured at \mathbf{x} in the inertial frame is given by:

$$\mathbf{u} = \dot{\mathbf{x}} - \mathbf{R}(\theta){}^{ASV}\tilde{\mathbf{v}} = \begin{bmatrix} \dot{x} \\ \dot{y} \end{bmatrix} - \mathbf{R}(\theta) \begin{bmatrix} v_A - d_A\omega \\ v_B - d_B\omega \end{bmatrix}. \quad (4.3)$$

where $\mathbf{R}(\theta)$ denotes the 2×2 planar rotation matrix and ω denotes the vehicle's angular velocity. In summary, (4.3) is used to obtain the flow velocity in the inertial frame using the onboard flow sensors and vehicle's state.

It is important to note that while the vehicle kinematics are modeled as a unicycle model with no sideslip (given by (2.1)), it has been observed in practice that the vehicle does experience some sideslip. As such, while the component of the flow velocity perpendicular to the vehicle's travel direction should theoretically be 0 cm/s at all times, in practice, this component is measured to obtain a better estimate of the flow velocity. Furthermore, (4.3) provides a good estimate of the flow velocity at \mathbf{x} as long as flow features of interest are large with respect to the vehicle's size. Lastly,

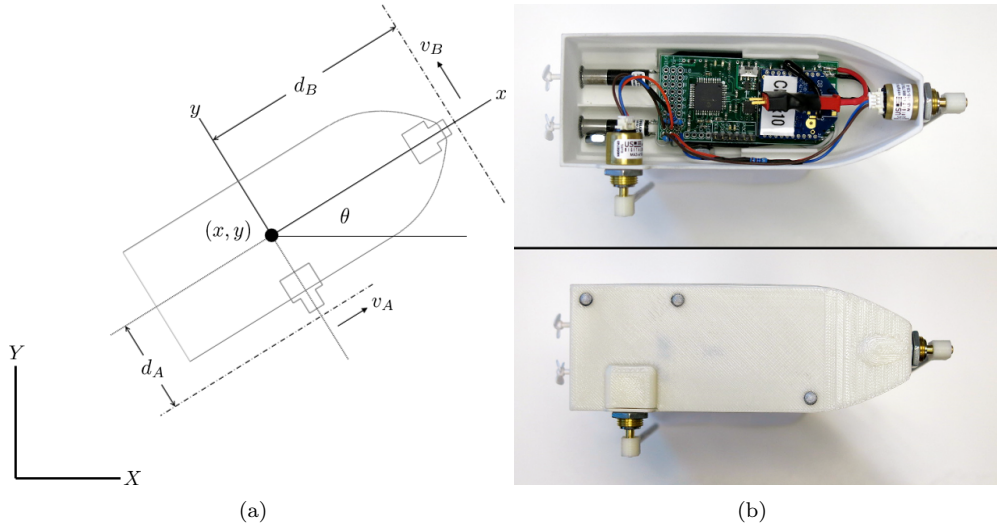


Figure 4.7: (a) Diagram of mASV in global XY frame. (b) Top view photos of a typical mASV demonstrating the locations of the two flow sensing encoders and retro-reflective markers.

since the flow field is assumed to be predominantly 2D, the aluminum rods were designed to only extend into the top layer of the water in the tank. As such, the measurements are only valid for the upper layer of the tank.

Flow Sensor Calibration

Let the angular displacement of flow sensors A and B be written as ϕ_A and ϕ_B , respectively. Recall that flow sensor A measures flow speed in the direction of travel of the mASV, and sensor B measures flow speed perpendicular to the direction of travel of the mASVF. A typical mASVF with encoders mounted is pictured in Figure 4.7(b). The relationship between encoder angle and flow velocity was determined empirically by driving an mASVF in a straight line at a constant velocity in still water, i.e., with $\mathbf{u} = 0$. In this configuration, flow sensor A , which is aligned with the forward motion of the mASVF, experiences a velocity identical to the actual velocity V of the vehicle so that $v_A = V$. The actual velocity of the vehicle, V , was measured using the external motion capture system. This procedure was repeated for various velocities up to the maximum speed of the vehicle. Figure 4.8(a) summarizes the results from the various runs, with velocities ranging from 0 m/s to roughly 0.12 m/s. From the data shown in Figure 4.8(a), the relationship between encoder angle and flow velocity is, to a good approximation for small angles, quadratic. Therefore, a quadratic function was fitted to the data, as shown in Figure 4.8(a), to obtain a relationship between encoder angle

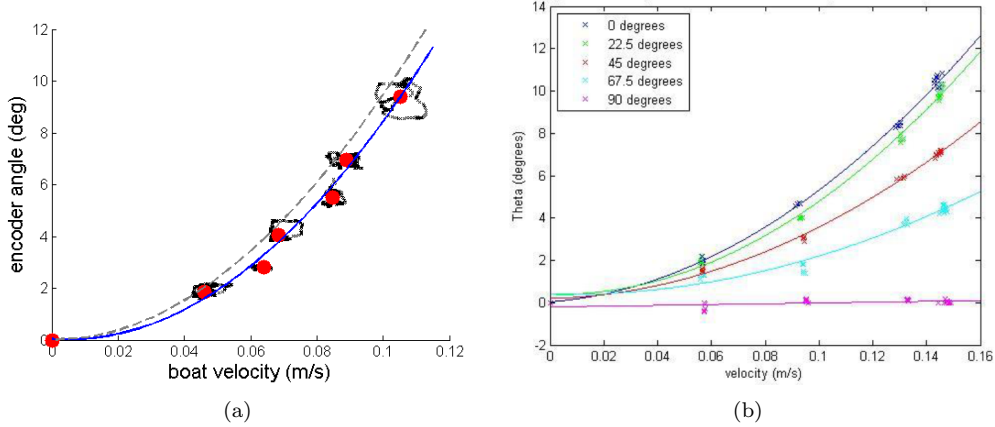


Figure 4.8: (a) Encoder A angular displacement vs. actual mASV forward velocity (in still water). The data points for each run are shown in black, the red dots indicate the mean values for each run, and the blue curve is a quadratic fitted to the mean data. The gray dashed line is the theoretical predicted relationship given by (4.2). (b) Flow sensor data from linear actuator with sensor mounted at various angles with respect to flow direction. Individual data points are shown as well as quadratic fits for each angle.

and flow speed. Using this function, measured velocities v_A and v_B can be obtained as functions of ϕ_A and ϕ_B , respectively.

Flow Sensor Evaluation

To evaluate the sensor's ability to extract the directionality of the surrounding flow field, the two flow sensors were also mounted on a linear actuator in the same mutually orthogonal configuration, as shown in Figure 4.9. The linear actuator was driven at various constant speeds with the sensors mounted at a variety of angles with respect to the direction of motion. The objective is to simulate the sensors mounted on a vehicle deployed at various angles in a constant linear flow field. The velocity of the sensor platform was measured using the external motion capture system and the results are shown in Figure 4.8(b). Note that the submerged length of the rod for the results shown in Figures 4.8(a) was different from the results shown in Figure 4.8(b), so the correlation between angle and flow speed is scaled differently for these two sets of results.

4.2 Flow Tanks

Simulations of the tracking strategy using analytical flow models provide a useful tool for evaluating its efficacy and robustness, but only cursorily take into account the natural stochasticity and

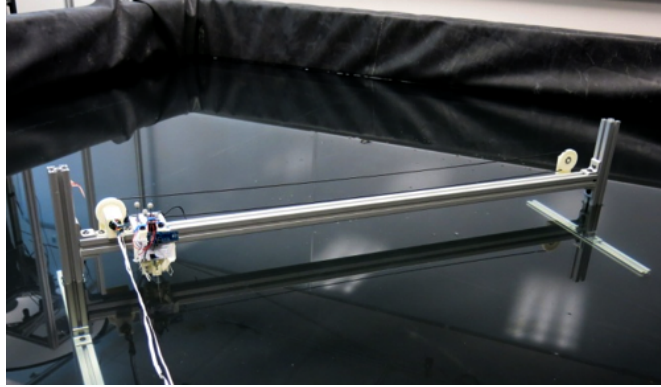


Figure 4.9: Linear actuator used to evaluate the flow sensors.

Table 4.4: Comparison of LoRe, HiRe, and MR flow tanks.

	LoRe Tank	HiRe Tank	MR Tank
Re regime	$10^1 \sim 10^3$	$> 10^4$	$> 10^4$
Size	$0.1 \times 0.1 \times 0.02 \text{ m}^3$	$0.6 \times 0.6 \times 0.3 \text{ m}^3$	$3.0 \times 3.0 \times 1.0 \text{ m}^3$
Medium	water/glycerol-water mix	water	water
Typical liquid depth	2 cm	14 cm	30 cm
Flow driving devices	Two banks of 8 cylinders	12+ indep. cylinders	12+ indep. cylinders
Flow measurement	Laser PIV	Visible PIV/PTV	none

aperiodicity of ocean flows. Using actual ocean data for simulation is a step further, and indeed an important component for evaluating the tracking strategy in flows of interest for AUV deployment. However, the available ocean data is often sparse with respect to the spatial and temporal scales of actual mobile robots. Furthermore, one cannot control the features prominent in ocean flows, and the dynamic interaction between the flow and deployed robotic vehicles requires more complex dynamics modeling of the vehicles.

It is therefore desirable to be able to generate and measure complex, controlled flows in a laboratory setting. To this end, a lab-scale flow testbed was developed in order to generate controllable flow fields that exhibit the transport-controlling features commonly seen in the ocean. The flows created by the testbed exhibit stochasticity and complex features, but have been shown to produce persistent flow features similar to those found in analytical models and the ocean [24].

The flow tanks that make up the experimental testbed include the 8 cm square LoRe tank, the 60 cm square HiRe tank, and the 3 m square MR tank. A comparison of the three types of flow tanks is presented in Table 4.4. Because of the previously-discussed useful properties of wind-driven double-gyre flow model, the objective is to develop a laboratory testbed capable of generating flows

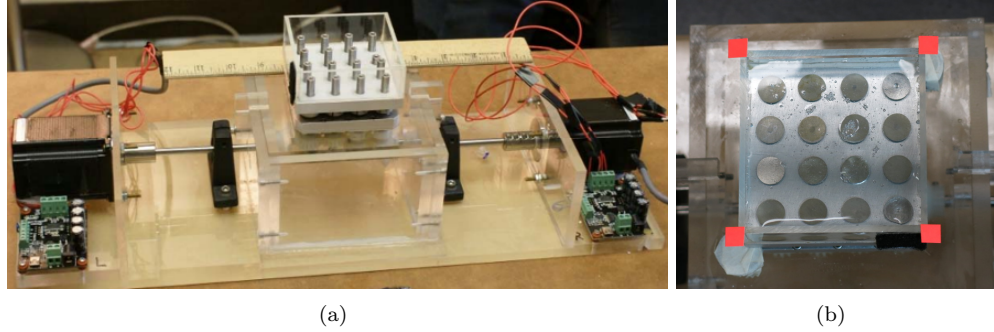


Figure 4.10: The LoRe tank, showing (a) independently controlled motors and (b) bank of spinning cylinders.

similar to (2.3). This flow is induced in the tanks using spinning cylinders arranged in a multi-gyre grid. In the LoRe tank, this flow is induced by two banks of spinning cylinders controlled by stepper motors, and in the HiRe and MR tanks, individually controlled motor/cylinder pairs are employed.

Particle image velocimetry (PIV) is used to extract the 2D surface velocity fields and the data is then processed. The experimental surface flow data is compared with the similar 2D analytical wind-driven double gyre model, and the existence of manifolds and coherent structures in the flow is verified [24].

4.2.1 LoRe Tank

The LoRe tank (the smallest tank) is designed to impose precisely formed perturbations onto controlled and realistic flows in the low Reynolds number regime. An 8 cm square transparent tank is filled to a depth $d = 2$ cm with a glycerol-water mix and driven by a 4×4 lattice of submerged disks mounted to an array of shafts linked by gears. The apparatus is designed so that the two adjacent 4×2 sets of disks have separate stepper motors, controllers, and gears such that they may be independently driven at any time-dependent angular velocity function from a simple Matlab code. High quality PIV is obtained using laser light sheet illuminated $50 \mu\text{m}$ diameter tracer particles and a high speed video camera. The LoRe tank is pictured in Figure 4.10.

4.2.2 HiRe Tank

While the LoRe tank is useful in precisely measuring flow-dependent transport features, it is of limited use when considering the interaction of AUVs and ASVs with transport. Creating a more realistic experimental platform where multiple robots may track features in complex time-dependent

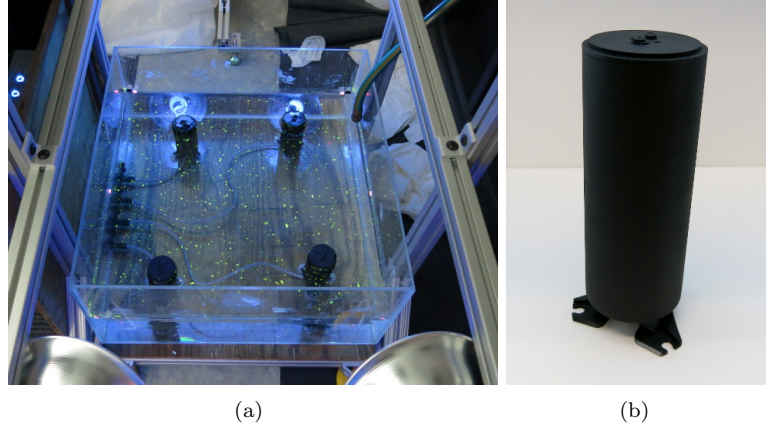


Figure 4.11: (a) The HiRe tank and (b) a flow driving cylinder.

flows in which they are immersed requires a larger flow field in which more unsteady, higher Reynolds number flows can be generated, still with some degree of control over perturbations. At Reynolds numbers in the range $\text{Re} > O(10^4)$, sheared flows such as multiple gyres will exhibit strongly nonlinear response to driving and display complex, time-dependent flow patterns. Nevertheless, the coarse features of the flows, such as the mean sizes and locations of the gyres and their boundaries, must be able to be controlled. Ultimately, the laboratory experiment must also accommodate the deployment of a small network of robots within the flow. The dominant flow features must therefore remain large enough in scale that the trajectory of a robot within the flow is approximately that of a tracer.

To achieve this, a $60 \times 60 \times 30 \text{ cm}^3$ acrylic flow tank, pictured in Figure 4.11(a), was built. The tank is filled with water to a depth of 14 cm. Flow fields in both the HiRe tank and the MR tank (described below) are generated using reconfigurable arrays of DC geared motors each mounted to acrylic cylinders of varying diameters and lengths (see Figure 4.11(b)). The motors are equipped with magnetic encoders to enable closed-loop control of the motor speeds. Each motorized cylinder is then mounted perpendicular to the bottom of the tank. The dynamics of the flow field are changed by setting the speed and direction of the various motorized cylinders. A nearly time-independent flow field can be created by placing the motorized cylinders on a grid and setting the cylinders to rotate at the same constant speed, but each in an opposing direction to its immediate neighbors. Time-varying flow fields can be generated by periodically changing the direction and the speed of specific cylinders in the grid.

In the HiRe tank, particle imaging velocimetry (PIV) and/or particle tracking velocimetry (PTV)

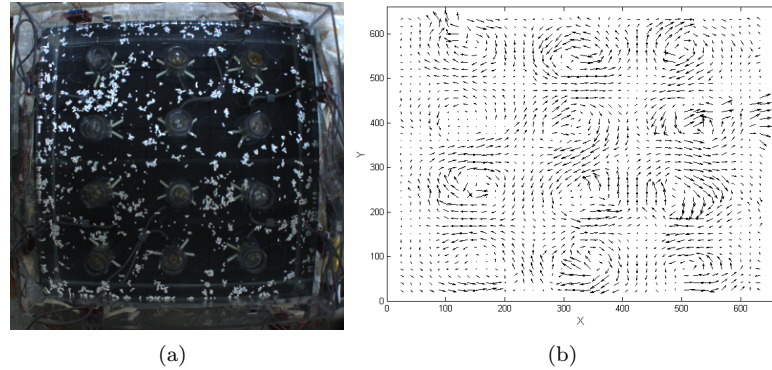


Figure 4.12: (a) Experimental setup of flow tank with 12 driven cylinders. (b) Flow field obtained via particle image velocimetry (PIV).

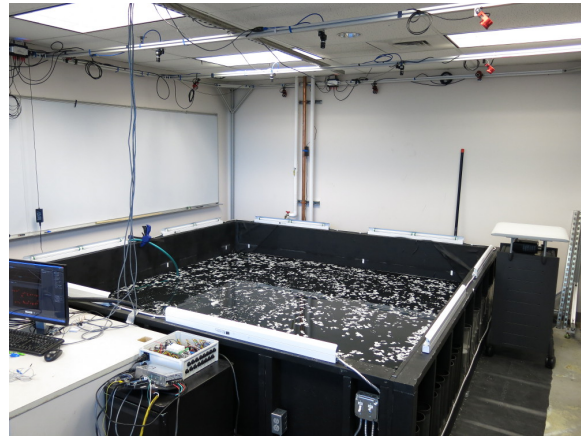


Figure 4.13: MR tank and overhead motion capture camera system.

is used to track the surface flow field [3] with two color cameras and spherical fluorescent tracer particles 0.3–0.35 mm in diameter. The raw images are then processed using the open-source Matlab PIV Toolbox [1] to extract the surface velocities of the fluid. A sample frame of the experimental setup with a 4×3 grid of cylinders is shown in Figure 4.12(a) and the extracted velocity field is shown in Figure 4.12(b).

The measured velocity fields from the HiRe tank exhibit coherent structures suitable for evaluation of the tracking strategy. Simulation and experimental results using data from the HiRe tank are presented in Sections 5.4 and 6.1.3, respectively.

4.2.3 Multi-Robot (MR) Tank

The goal of this work is to improve the autonomy of underwater vehicle dynamics by exploiting kinematically based transport features in oceanic flows. As such, the laboratory experiments must be scaled to accommodate the deployment of a small network of robots within the flow field. While both the HiRe and MR tanks operate in flow regimes with $\text{Re} > O(10^4)$, the MR Tank is specifically designed to accommodate multiple mASVs and up to a 6×6 grid of rotating cylinders with diameters in the range 5 – 15 cm. The MR tank is also equipped with an OptiTrack motion capture camera system which provides real time rigid body tracking of the ASVs at 120 Hz. This raw pose data is low pass filtered and differentiated to obtain position, orientation, and their respective rates for each vehicle in the tank. The MR tank is pictured in Figure 4.13.

4.3 Summary

This chapter described an experimental testbed developed at the Scalable Autonomous Systems Laboratory. The system comprises two main components: a set of three flow tanks and a fleet of several autonomous surface vehicles (ASVs). The experimental testbed described in this chapter is used to experimentally evaluate the coherent structure tracking strategy described in Chapter 3. The utility of the testbed lies in the ability to evaluate the tracking strategy with real autonomous vehicles in controllable flows that behave similarly to geophysical flows. This is a first step toward actual deployment of robotic vehicles into geophysical flow environments such as the ocean.

5. Simulation Results

This chapter presents simulations for tracking manifolds and Lagrangian coherent structures of analytical flow models, flows created in the lab testbed described in Chapter 4, and real ocean flows.

5.1 Methodology and Implementation

The simulations presented here were implemented in Matlab. To simulate the vehicle motions, the kinematic model given by (2.1) was used along with a simple Euler integration method with a time step dt . In this single integrator model, the position of a vehicle at time step $n + 1$ is given by:

$$x_{n+1} = x_n + (V_n \cos \theta_n + u_n) dt \quad (5.1a)$$

$$y_{n+1} = y_n + (V_n \sin \theta_n + v_n) dt \quad (5.1b)$$

Recall that V_n and θ_n are taken to be control inputs. In addition to the simulation period dt , the simulated vehicles sample the underlying flow field and compute control inputs at a slower frequency. This sampling and control period dT is typically about three times longer than the integration period dt . This reflects the fact that the measurement frequency for an actual sensor on a deployed vehicle is typically upper-bounded. Increasing the integration frequency (by decreasing the simulation time step dt) results in better simulation accuracy at the expense of increased computation time.

5.2 Tracking with the Wind-Driven Double Gyre Model

The wind-driven double gyre model discussed in Section 2.2 provides a convenient model to evaluate the effectiveness of the tracking strategy in simulation. Simulation results with the static double gyre model are presented in Section 5.2.1, while results with the time varying double gyre model are presented in Section 5.2.2. The effect of sensor noise on tracking is discussed in Section 5.2.3.

5.2.1 Static Double Gyre Model

In this section, the underlying vector field is given by (2.4). Note that (2.4) is not a conservative vector field, since $\frac{\partial \dot{x}}{\partial y} \neq \frac{\partial \dot{y}}{\partial x}$. Therefore, it is not guaranteed that the robots will maintain a saddle

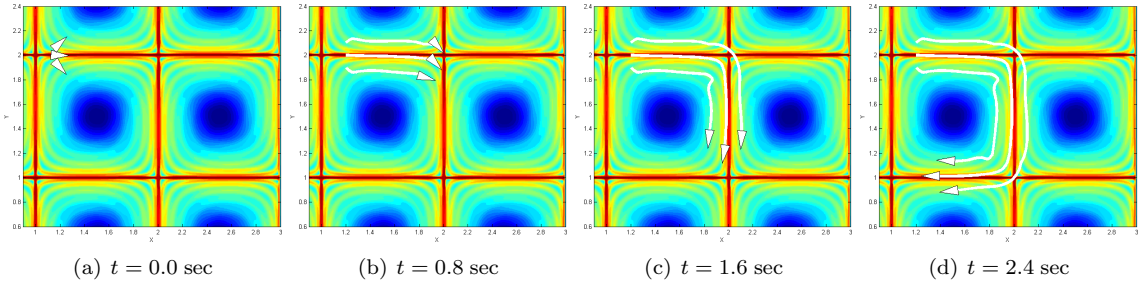


Figure 5.1: Trajectories of a team of 3 robots tracking the stable/unstable manifolds of the static double gyre system given by (2.4) with $A = 1$ and $s = 1$. The FTLE integration time is $T = 4$ sec.

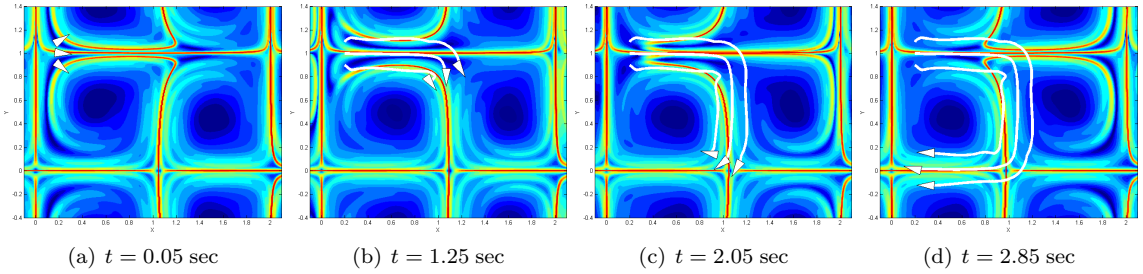


Figure 5.2: Trajectories of a team of 3 robots tracking the coherent structures of the time-varying double gyre system given by (2.3). The FTLE integration time is $T = 4.5$ sec.

straddling formation across the invariant manifolds. However, simulation results have suggested that the team is able to effectively maintain the formation across the boundaries.

Figure 5.1 shows a team of three robots tracking manifolds of the static double gyre model, with the corresponding FTLE field overlaid. Because this system is time invariant, the boundaries are indeed stable and unstable manifolds of the fixed points at the edges of each gyre.

5.2.2 Time Varying Double Gyre Model

In this section, the underlying flow field is given by (2.3). In this time varying double gyre model, the separatrix between gyres in the flow field undergoes a periodic oscillation in the x direction; that is, it moves side-to-side as the flow evolves, with a frequency given by the term $\omega/2\pi$ and an amplitude given by ε . This separatrix coincides with a ridge of high FTLE values, so it is defined as a Lagrangian coherent structure.

The goal of these simulations is for the team of three robots to track the coherent structures in this time varying flow, including the central oscillating separatrix. Figure 5.2 shows trajectories of

three robots attempting to track these coherent structures, along with the overlaid FTLE field. In this simulation, the parameters in (2.3) are given by $A = 0.2$, $\mu = 0.005$, $\varepsilon = 0.1$, $\Psi = 0$, $\omega = \frac{\pi}{3}$, and $s = 1$.

5.2.3 Modeling Sensor Noise

Measurements from real sensors are often corrupted by noise. To simulate the effect of sensor noise in an actual robotic system, the flow velocities as measured by each robot are given by:

$$u_i = \dot{x} + \eta_{x_i}(t), \quad (5.2a)$$

$$v_i = \dot{y} + \eta_{y_i}(t). \quad (5.2b)$$

for $i = \{L, C, R\}$ where \dot{x} and \dot{y} are given by (2.3) and where $\eta_{x_i}(t)$ and $\eta_{y_i}(t)$ describe uncorrelated stochastic white noise terms with mean zero and standard deviation $\sigma = \sqrt{2I}$, for noise intensity I . It should be noted that these noise terms are independent and identically distributed. This is because it is assumed that there are two distinct sensors measuring the two flow velocity components.

A series of simulations was performed with varying noise intensities I in (5.2). Figure 5.3 shows the resulting tracks for different values of I . In these simulations, the remaining parameters are identical to the simulation presented in Section 5.2.2. In these simulations, the mean component velocity magnitude of the entire flow is 0.42, and the maximum component velocity magnitude is 0.76. It can be seen that the team tracks the boundaries reasonably well even with $I = 0.05$. This corresponds to a standard deviation of 0.32 for the noise, which is almost the magnitude of the mean velocity in the flow. This shows that even with significant noise, the team is still able to maintain a straddling formation across the boundary.

To further quantify the effect of noise on the tracking strategy, many tracking runs were simulated for varying values of I (with all parameters identical to the previous simulations) and the number of instances (indicated by N_{fail}) for which the team failed to maintain a valid straddling formation after 1.5 seconds was recorded. The results are tabulated in Table 5.1.

5.3 Tracking with Formation Control

In simulations with only 3-robot teams, it has been observed that occasionally the interpolation of the velocity field is inaccurate in the regions between the robots. This can lead to an erroneous

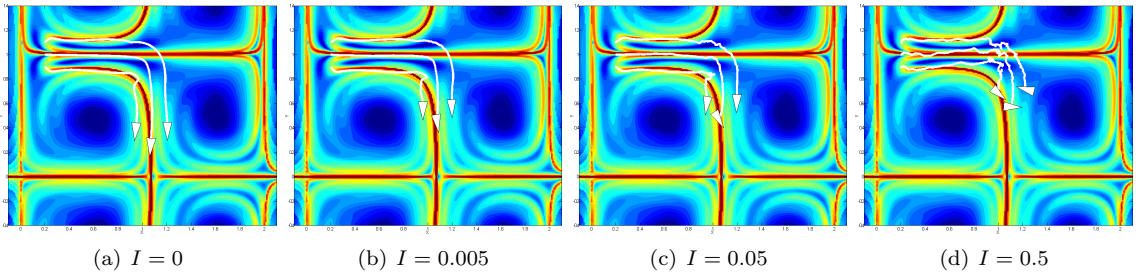


Figure 5.3: Trajectories of teams of 3 robots performing tracking as in Section 5.2.2, but with increasing sensor noise intensities. In all frames, $t = 1.7$ and measurement noise is modeled as zero-mean Gaussian with $\sigma = \sqrt{2T}$. It can be seen that tracking fails with sufficiently high measurement noise.

Table 5.1: Varying noise intensities and number of failures to maintain straddling formation.

Noise Intensity I	N_{fail} (out of 50)	Percent Success
0.001	8	84 %
0.005	13	74 %
0.05	16	68 %
0.1	21	58 %
0.5	33	34 %

estimate of the location of the manifold or coherent structure, and can cause the team to fail to maintain a proper straddling formation. Since the tracking controller is predicated on the team's ability to collectively sample the flow field and accurately interpolate it over a region, adding more sensing agents can improve the interpolation and result in a better estimate of the underlying flow field.

The tracking strategy with formation control is described in Section 3.2. In this case, the 3 leader agents behave similarly to the 3 agents in the normal tracking strategy, and $n - 3$ follower agents remain within a triangle defined by the leader agents using a formation control strategy that treats the agents as particles in an evolving continuum. This formation control strategy, described in [27–29], provides a simple framework for the followers’ control actions, and ensures that they remain inside the leading triangle and avoid collisions with each other.

Figure 5.4 shows a team of 3 leader agents and 5 follower agents tracking a manifold of the vector field given by

$$\mathbf{u} = -a\nabla\phi - b\nabla\times\psi \quad (5.3)$$

where $a, b > 0$ and ϕ is a potential function such that $\phi(\mathbf{x}) = 0$ for all $\mathbf{x} \in B_*$ and $\phi(\mathbf{x}) < 0$ for any

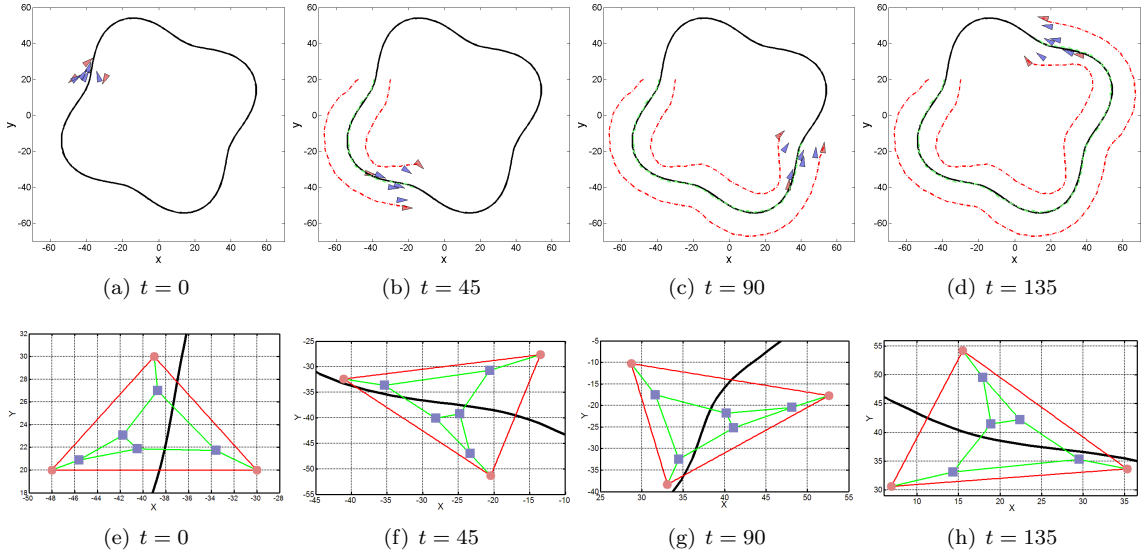


Figure 5.4: Snapshots of the positions of agents at various times while tracking manifolds of the vector field given by (5.3). The top row (a)-(d) shows the team tracking the boundary, and the zoomed-in images in the bottom row (e)-(h) show the positions of the agents at the same times as (a)-(d) with the communication graph of the team overlaid. Leader agents are shown in red, while follower agents are shown in blue. The solid black line is the boundary being tracked.

$\mathbf{x} \in \mathbb{R}^2/B_*$. The vector ψ is a 3×1 vector whose entries are given by $[0, 0, \gamma(x, y)]^T$ where $\gamma(x, y)$ is the curve describing the desired boundary. It can be seen that the team successfully maintains a straddling formation across the boundary.

This multi-agent technique has also been simulated using the time varying double gyre model given by (2.3). Figure 5.5 shows trajectories of a team of 8 agents tracking coherent structures of (2.3).

5.4 Tracking using HiRe Tank Data

Figure 5.6 shows the use of the control strategy described in Chapter 3 to track coherent structures in the flow generated by the experimental HiRe tank described in Section 4.2.2. In these experiments, all the rotating cylinders were set at constant speed; as such, the coherent structures exhibited in the flows are approximately time-independent but stochastic. Quantitative analysis and comparison of the experimental flow data with the analytical gyre model shows good correspondence and is described in [24].

While the team can be seen to occasionally traverse across regions with local maximum FTLE measures, the team quickly resumes straddling another neighboring FTLE ridge. The most likely

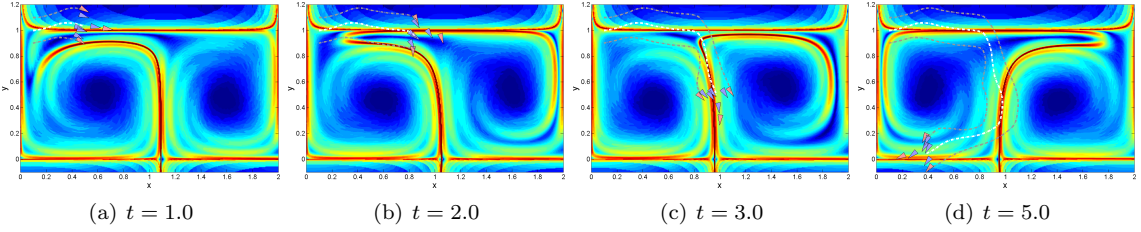


Figure 5.5: Trajectories of a team of 3 leader agents and 5 follower agents tracking the coherent structures of the time-varying double gyre system given by (2.3). The FTLE integration time is $T = 4.5$ sec.

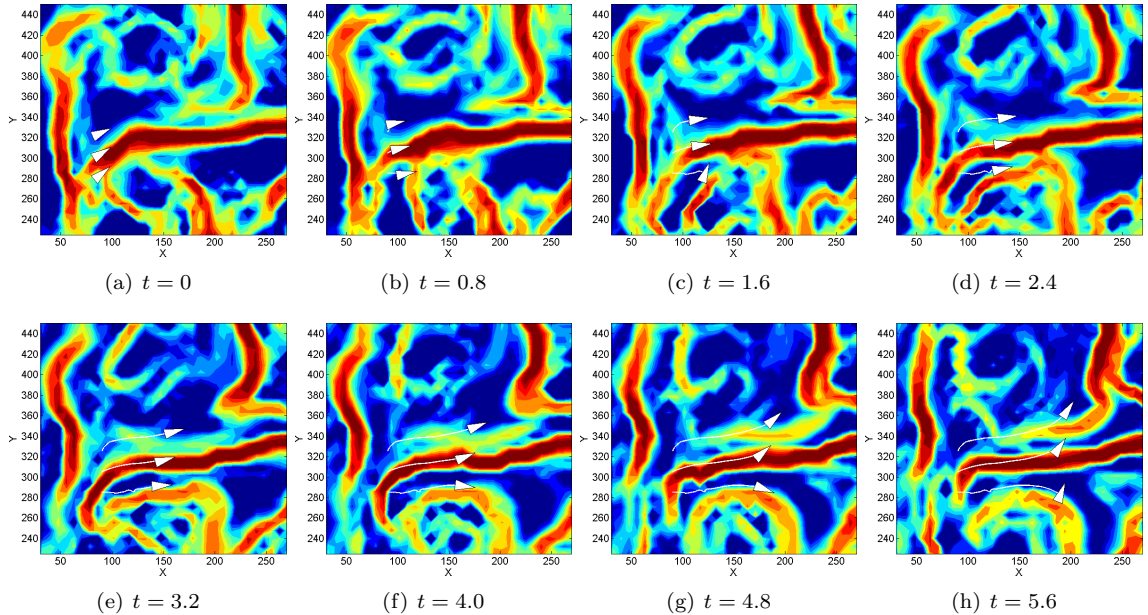


Figure 5.6: Trajectories of 3 simulated robots tracking a coherent structure using data obtained from the experimental testbed. In this simulation, the average velocity of the robots is slightly higher than the mean velocity of the underlying flow. To give a sense of time scale, tracer particles take roughly 10 seconds to recirculate through the gyres.

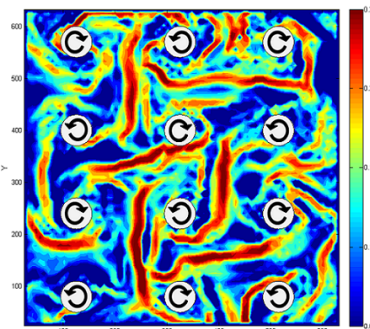


Figure 5.7: Approximate positions of the tank cylinders, and their rotational directions, in relation to the computed FLTE field.

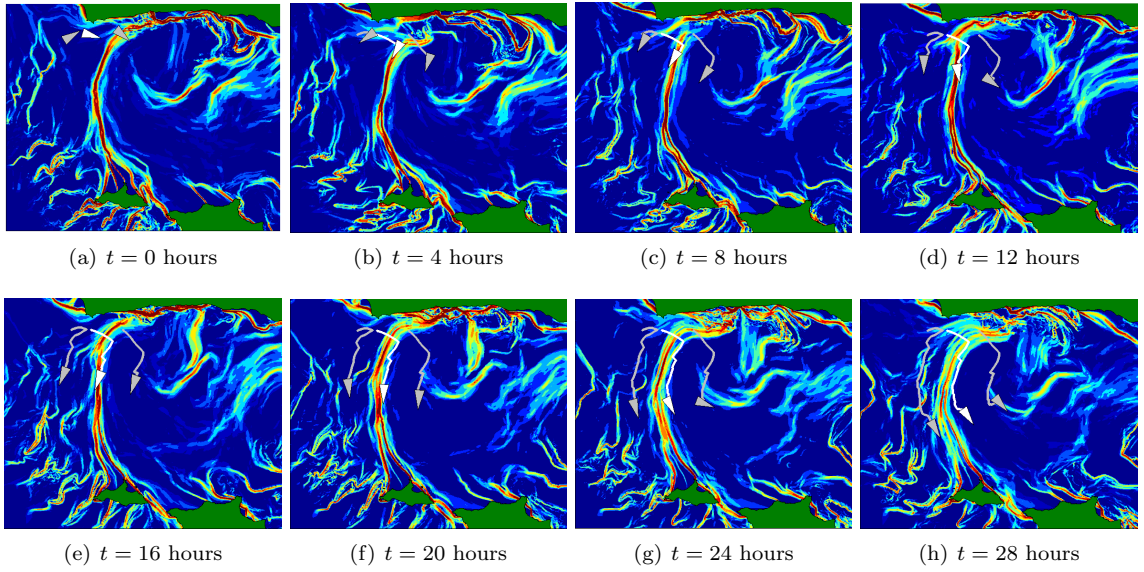


Figure 5.8: Three simulated robots tracking a Lagrangian Coherent Structure off the coast of California over a 28 hour window.

explanation for this temporary break in the saddle straddling formation is that the team approached a local saddle point in the flow. As the team approaches the saddle point from one side, the other side of the saddle point in the flow field reverses direction. As such, the robots would be temporarily pushed away from the saddle point until they find another manifold to track. This is supported by the positions of rotating cylinders in relation to the FTLE ridges, which is shown in Figure 5.7. Note that saddle points are located in the middle of every set of four rotating cylinders.

5.5 Tracking using Ocean Flow Data

The coherent structure tracking strategy was also implemented using real ocean flow data. Specifically, the Santa Barbara Channel along the California coast is studied. This area is instrumented with several high-frequency radar stations which provide hourly surface current measurements on a 2 km grid, as described in Section 2.3. Figure 2.5 shows a snapshot of the measured velocity field and the associated FTLE field for the Santa Barbara Channel during a strong eddy event in May 2012. This area is interesting because there is a recurring small-scale eddy (roughly 40 km in diameter) which appears between the Channel Islands and the mainland. This eddy results in an area of highly divergent flow straining between the mainland and San Miguel Island, which can be easily seen as a ridge of high FTLE values in Figure 2.5(b).

The tracking strategy was simulated in this region over a 28 hour window using data from 16 May 2012 08:00:00 GMT to 17 May 2012 12:00:00 GMT. Figure 5.8 shows the team of three robots tracking a strong LCS stringing between the mainland and San Miguel Island. Even with a relatively poor initial guess of the LCS location, the team quickly forms a straddling formation and tracks the strong LCS while traversing southward. Several instances have been observed during which this type of persistent LCS remains across the mouth of the Santa Barbara channel for several days. Because of its long duration, revealing LCS such as this one is useful for predicting transport phenomena at useful time scales.

5.6 Summary

In this chapter, a general methodology for computer simulations of the tracking strategy described in Chapter 3 was presented. Simulations were carried out on a variety of vector fields, including time invariant and time varying periodic gyre models, vector fields generated by the experimental HiRe tank described in Section 4.2.2, and real ocean data from the California coast. The results of these simulations were presented alongside computed FTLE fields to evaluate the effectiveness of the strategy at maintaining a formation which straddles LCS, or ridges of high values in the FTLE field. In addition, the effect of sensor noise was studied and several simulation runs were presented for varying sensor noise intensities. In most cases, the team of mobile sensing robots was able to successfully track the manifolds and/or coherent structures in each of the flows, at least for a limited period of time (as in the ocean flow data).

6. Experimental Results

This chapter presents experimental results using the testbed described in Chapter 4, which comprises three flow tanks and a fleet of two classes of autonomous surface vehicles.

6.1 MR Tank - Still Water

The mASV class vehicles, pictured in Figure 6.1(b) do not have onboard flow sensing capabilities, so it is not possible to experimentally implement the LCS tracking strategy in its fullest sense. However, it is possible to generate artificial sensor outputs for each mASV in the MR tank as if they were equipped with actual flow sensors, then execute the appropriate tracking controller for each vehicle.

These ‘artificial’ flow sensor measurements are generated based on the position of the vehicle in the MR tank and an underlying flow vector field which is scaled up to match the dimensions of the MR tank. An example of such a scaled up flow field is shown in Figure 6.1(a), in which the vector field is simply a 3×3 static gyre model, similar to (2.4). To make this experimental setup more realistic, noise can be added to the artificial flow sensor outputs to reflect the fact that sensors are inevitably noisy.

In the experiments described in this section, there are no flow driving cylinders in the MR tank. Even though the water in the MR tank is quiescent, the utility of this form of experimental verification lies in the addition of real-world fluid flow phenomena affecting the vehicles while they attempt to track coherent structures in the artificial flow field. Also, the small-scale mASVs behave similarly in a kinematics and dynamics sense to larger ocean-going autonomous vehicles.

6.1.1 Static Double Gyre Model

In this case, the experiment was performed in still water in the MR tank where the robots’ flow sensor outputs were simulated, i.e., \mathbf{u}_i is given by the time-invariant wind drive double-gyre model described by (2.4) with $A = 0.2$ and $s = 1.5$. Even though there were no actual flows in the MR tank during these experiments, the motion of the mASV team was enough to generate a background flow in the MR tank which can impact the tracking strategy, making this scenario more realistic than pure simulations. Figure 6.2(b) shows the trajectories of 3 mASVs in the MR tank. It can

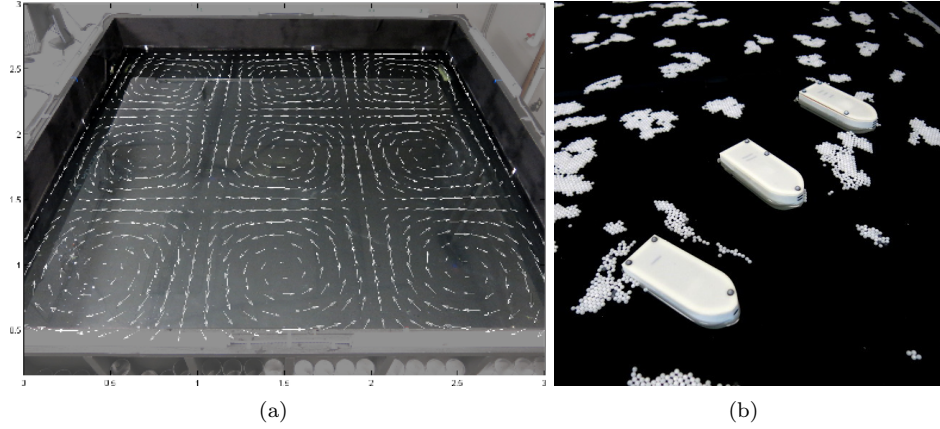


Figure 6.1: (a) Photograph of the MR tank with a sample 3×3 static double gyre vector field overlaid and (b) photograph of three MASVs in the MR tank. Visible in (b) are the unique patterns of retro-reflective markers for overhead motion capture tracking.

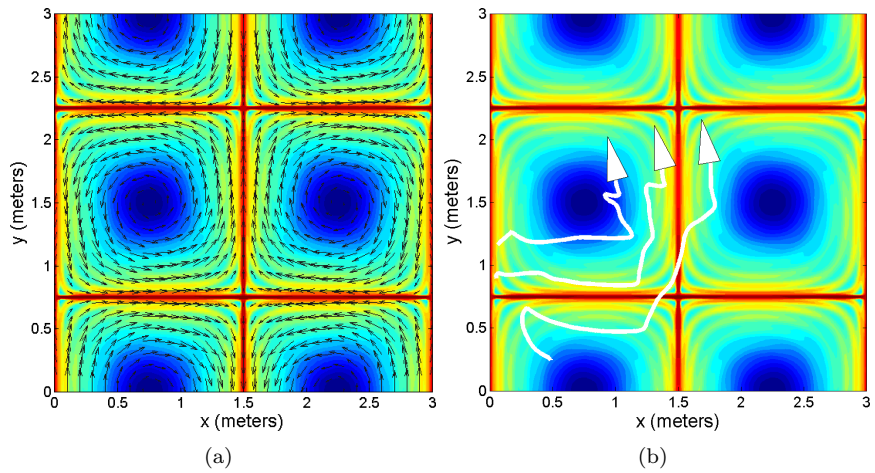


Figure 6.2: (a) Time invariant double gyre flow field with FTLE field overlaid and (b) paths of a 3 mASVs in MR tank tracking LCS in a simulated time invariant double gyre flow with FTLE field overlaid.

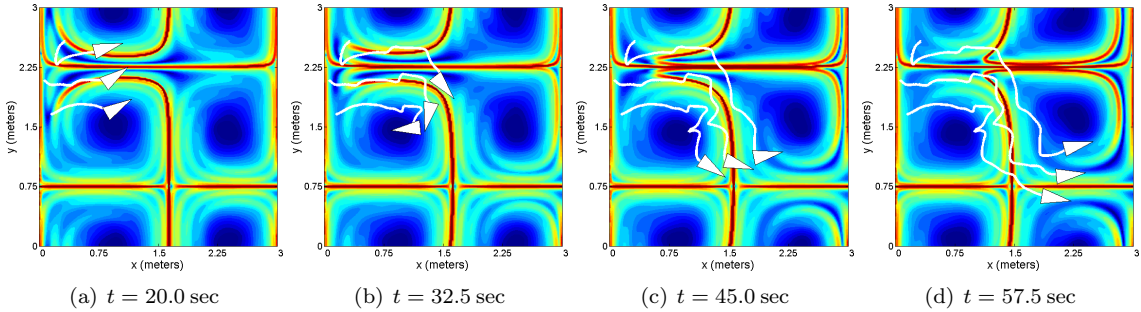


Figure 6.3: Paths of 3 mASVs in the MR tank tracking a time varying LCS of a simulated double gyre flow given by (2.3).

be seen that the robots remain in a straddling formation across the manifold, shown in red, until reaching a hyperbolic point in the flow. At this point, the team shifts to track another manifold in the flow. This behavior is desired since the team is always attempting to track a manifold or coherent structure, and it has been observed in previous simulation results [22].

6.1.2 Time Varying Double Gyre Model

The experiments for this case were performed in still water in the MR tank where the robots' flow sensor outputs were simulated using a *periodic* (instead of time invariant) flow model, i.e., \mathbf{u}_i is given by (2.3) with $A = 0.2$, $\epsilon = 0.1$, $\mu = 0.005$, $\omega = 0.05$, $\psi = 0$, and $s = 1.5$. Figure 6.3 shows the trajectories of the robot team while tracking the LCS (shown in red) in the flow. The vehicles were able to maintain a straddling formation across the moving LCS as can be seen in the middle of the figure.

Adding Simulated Sensor Noise

To emulate sensor measurement error/noise, a zero mean Gaussian noise was added to each robot's simulated flow sensor outputs. The underlying flow field is given by (2.3) with $A = 0.2$, $\epsilon = 0.1$, $\mu = 0.005$, $\omega = 0.05$, $\psi = 0$, and $s = 1.5$, similarly to Section 6.1.2. Figure 6.4 compares the robot trajectories for runs both with and without sensor noise. Even with a sensor noise standard deviation of 0.14 m/s, which is equal to about 25% of the maximum velocity in the flow, the team is still able to track the time-varying LCS.

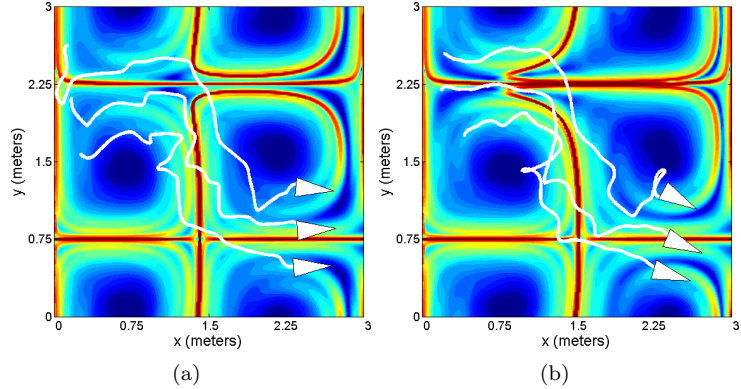


Figure 6.4: Paths of 3 mASVs in the MR tank tracking a time varying LCS of a simulated double gyre flow given by (2.3) for two different experimental runs. Run (a) was performed without simulated sensor noise, while run (b) was performed with simulated sensor noise. The additive sensor noise was modeled as a zero-mean normal distribution with a standard deviation of 0.14 m/s.

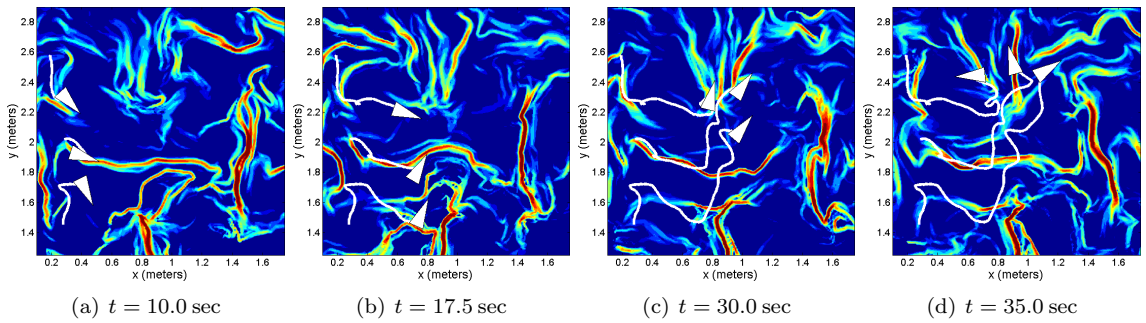


Figure 6.5: Paths of 3 mASVs in the MR tank tracking a time varying LCS from actual flow data obtained in the High Reynolds number (HiRe) tank.

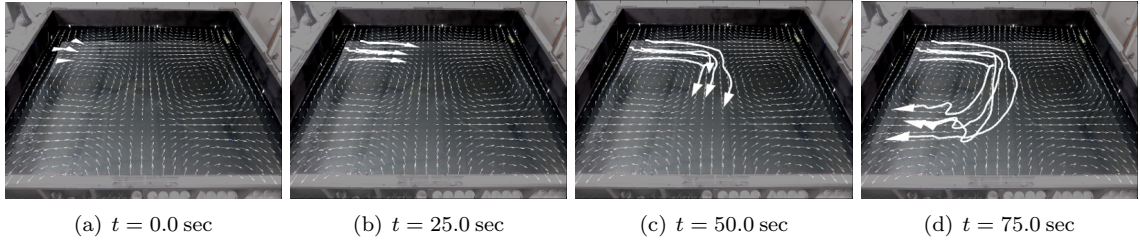


Figure 6.6: Paths of 4 mASVs in the MR tank tracking manifolds of a simulated double gyre flow given by (2.4).

6.1.3 Scaled-up HiRe Tank Data

In this case, a time-invariant flow field was created in the smaller HiRe tank using a grid of 3×4 flow driving cylinders. The data was collected, scaled, and played back during the manifold/LCS tracking experiment. As such, the flows “experienced” and “measured” by the mASVs were actual flows, however, the flows were created within the HiRe tank. In other words, the robots’ simulated flow sensor outputs were given by scaled-up actual flow data. Figure 6.5 shows that the team tracks an LCS while moving left to right, then after reaching a hyperbolic point in the flow begins to track another LCS while moving upward in the figure.

6.1.4 Double Gyre Model with Larger Teams

In addition to the three robot tracking strategy (presented in Section 3.1), the multi-robot leader-follower tracking strategy presented in Section 3.2 was also evaluated experimentally. Figure 6.6 shows a view of the MR tank including the underlying static double gyre vector field and paths of 4 agents tracking the invariant manifolds. Only one follower agent was deployed for these experiments – this is because an odd number of followers is required as a condition of the formation control strategy, and three or more follower boats would create problematic clutter and frequent inter-agent collisions in the MR tank. Deployment of the boats into a larger flow tank, with larger simulated flow features, would make the experimental setup more amenable to larger numbers of follower agents.

6.2 MR Tank - Generated Flow

Figure 6.7(a) shows the MR tank with 4 flow driving motors arranged in a double gyre formation. The motors are actuated such that the flow is similar to the static double gyre given by (2.4). In this case, a nearly time invariant multi-gyre flow was generated in the MR tank, and a pair of mASVFs

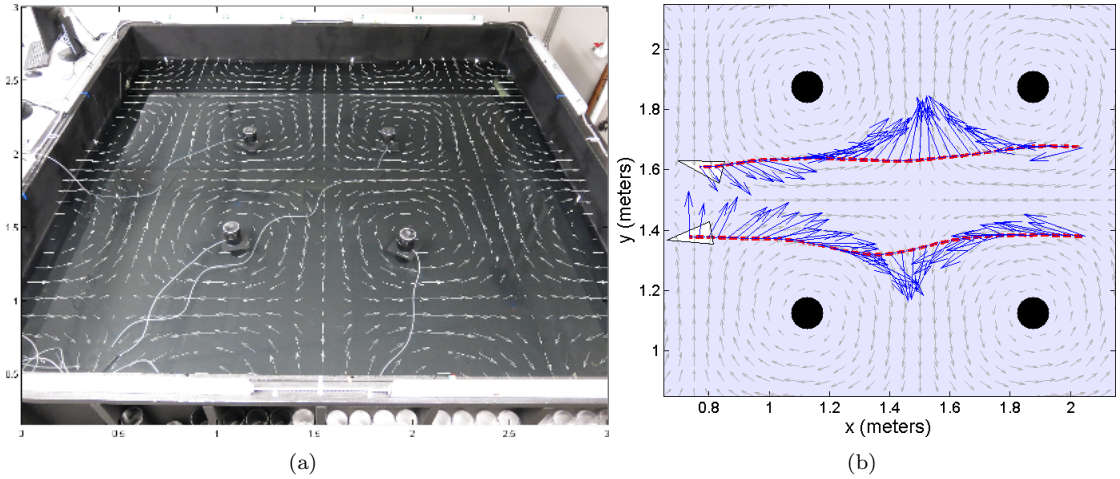


Figure 6.7: (a) Four spinning cylinders in the MR tank used to create a gyre like flow (overlaid) and (b) the paths of two mASVs moving through the flow while sampling the local flow velocity with onboard sensors. The trajectories of the mASVs are shown as dashed red curves and the flow measurements are shown as blue arrows. In both figures, the intended underlying flow field is shown in gray.

were deployed to sense the flow field while straddling the manifold/LCS between the two gyres. The experimental setup with 4 flow generating cylinders is shown in Figure 6.7(a). The trajectories of the two mASVs operating in the MR tank and their flow measurements, obtained with their onboard flow sensors, are shown in Figure 6.7(b).

It should be noted that the MR tank was designed to accommodate multiple robots and operate in flows that exhibit the complexity found in actual ocean flows. However, the flow velocity measurement capabilities of the MR tank are limited. Nonetheless, it is evident the MR tank is approximating the intended flows based on the data obtained using the HiRe tank. Indeed, the HiRe tank operates in a similar Reynolds number regime with similar flow complexity, but allows for high resolution PIV to validate the flow fields. By using the HiRe tank to guide the MR tank experiments, it is assured that the intended flow dynamics are being achieved.

6.3 Summary

This chapter presented experimental results in the testbed developed at the Scalable Autonomous Systems Laboratory. The experimental results are divided into those for which there is no flow in the MR tank and those for which an approximately time invariant double gyre flow similar to (2.4) is generated using spinning cylinders. In the first case, teams of mASVs in the MR tank attempt

to track manifolds and coherent structures using simulated sensor outputs given by scaled-up flow models. In the second case, two mASVFs attempt to accurately measure the underlying flow field. Results were presented as plots using position data from an overhead motion capture camera system.

7. Conclusion

This chapter presents some concluding remarks, including a summary of the contributions of this thesis and potential directions for future work.

7.1 Summary of Contributions

This work presented a detailed evaluation of the previously proposed manifold and coherent structure tracking strategy for a team of mobile sensing robots in two dimensional flows. The strategy was evaluated in computer simulations using a variety of analytical and measured flows, and with realistic effects such as sensor noise. In addition, this work described the development of a flow testbed comprising a series of flow tanks and two classes of novel, small-scale autonomous boats. This testbed was used to facilitate experimental validation of the strategy using measured data and actual robot deployment. The overall results of this effort have indicated that the tracking strategy, although designed for time invariant flows, can be used to track coherent structures in certain time dependent flows quite reliably.

The innate difficulty in tracking coherent structures in intensely time varying flows stems from the fact that an LCS, or more precisely an FTLE field, is in essence a *Lagrangian* metric (i.e., it depends on the evolution of trajectories in the flow over a fairly long time), but tracking is only based on instantaneous measures. This indicates that this strategy is perhaps best suited for regions and features of flows with weaker time dependence, yet which perhaps still exhibit stochastic effects. An example of such a feature as presented in this work is the persistent LCS spanning the Santa Barbara channel. Indeed, the persistence of such features makes their effect on the overall transport properties of the flow more prominent. For the purposes of this work, it would be less interesting to know the location of an LCS that vanishes very quickly and has little impact on the flow in a broad sense.

7.2 Future Work

Significant future work remains in order to realize the goal of deploying mobile robots into geophysical flows to track coherent structures in real time. Directions for future work are broadly divided into simulations and experiments.

7.2.1 Simulations

Regarding simulations, primary directions for future work would include using a variety of analytical flow models beyond the wind-driven double gyre model. Also, simulating the tracking strategy with more flow data from the testbed and analyzing different regions and time spans of the coastal ocean data would be fruitful. The main challenge in simulating more ocean regions is the requirement to treat most ocean data in an ad hoc manner. That is, different regions contain varying levels of data coverage and geological features such as coast lines and islands which present unique challenges from a computation perspective. The ocean data must be conditioned, sometimes heavily, before it is suitable for use in simulations or computation of FTLE fields.

Another interesting direction of future work would be an attempt to optimize in some sense the amount of energy used by the team while tracking the coherent structure, for example by attempting to maintain a near-zero velocity of the team with respect to the flow. In this way, the robots would simply allow themselves to be advected by the flow and only actuate to remain in a saddle straddling formation across the LCS. This is similar to the problem of fuel efficient navigation for weakly propelled vehicles [32], but it would not require full a priori knowledge of LCS locations.

Because the tracking strategy relies so heavily on the agents' ability to sample the flow and interpolate it over a region, it would be fruitful to further study the effect of sensor noise on the tracking strategy. Although this work studied the effect of additive Gaussian sensor noise, other types of noise may be present. Also, this work considered noise in the x and y velocity component measurements to be independent and identically distributed. In other types of measurement systems (e.g., wind vane style sensors), this assumption may not be valid.

A less direct area for future work includes extending the strategy to track LCS in three dimensional flows using autonomous underwater vehicles (AUVs). In n -dimensional flows, LCS are more difficult to define. It is sufficient, though, to consider them as codimension-1 manifolds in regions where there are no sources or sinks. Although most of the concepts discussed in this work extend quite naturally to n -dimensional space, simulations and experiments become more complex, and otherwise simple tasks such as computing FTLE fields become nontrivial due to the vast increase in data and computing resources required.

7.2.2 Experiments

Regarding experiments, an immediately evident direction for future work is to enable real time tracking of coherent structures in the MR tank using the mASVFs, which are equipped with onboard flow sensors. The primary difficulty in this effort stems from the practical issues encountered when operating the mASVFs. The requirement for two-way communication between each of the vehicles and a central computer necessitates the use of a dedicated radio network for each vehicle, increasing hardware required and decreasing communication robustness.

In addition, the process of extracting the global-frame flow field from the mASVF flow sensors and position/velocity data is inundated with noise. Aggressive low-pass filtering of measured data is required in order to reduce the effect of noise to a manageable level, introducing time delays and somewhat compromising the ability of the sensor setup to accurately measure the local flow. Creating stronger flows in the MR tank would serve to increase the signal-to-noise ratio of the flow sensor system on the mASVFs and would reduce the need for filtering, thereby improving the quality of flow sensing. The effort of real time tracking of coherent structures in the MR tank would also be greatly aided by the availability of flow velocity data using, for example, particle image velocimetry (PIV) or particle tracking velocimetry (PTV).

In addition, any real deployment of autonomous vehicles in the ocean would require an analysis of the sensitivity of the tracking strategy to time delays, potentially non-Gaussian sensor noise, and heterogeneity of sensors/vehicles; these issues have not been studied in this work.

Bibliography

- [1] MATLAB piv toolbox. <http://www.oceanwave.jp/softwares/mpiv/>.
- [2] Naitonal HF RADAR network - surface currents.
- [3] Ronald J. Adrian, Richard P. Wildes, Michael J. Amabile, Ann marie Lanzillotto, and Tzong shyng Leu. Particle imaging techniques for experimental fluid mechanics. In *In Proc. Conf. Comp. Vision Pattern Rec*, pages 969–975, 1991.
- [4] Juan C. Agui and J. Jimenez. On the performance of particle tracking. *Journal of Fluid Mechanics*, 185:447–468, 1987.
- [5] R. Doerner, B. Hübinger, W. Martienssen, S. Grossmann, and S. Thomae. Stable manifolds and predictability of dynamical systems. *Chaos, Solitons, & Fractals*, 10(11):1759–1782, November 1999.
- [6] Eric Forgoston, Lora Billings, Phillip Yecko, and Ira B. Schwartz. Set-based corral control in stochastic dynamical systems: Making almost invariant sets more invariant. *Chaos*, 21(013116), 2011.
- [7] V. M. Goncalves, L. C. A. Pimenta, C. A. Maia, B. Dutra, and G. A. S. Pereira. Vector fields for robot navigation along time-varying curves in n-dimensions. *IEEE Trans. on Robotics*, 26(4):647–659, 2010.
- [8] G. Haller. Lagrangian coherent structures from approximate velocity data. *Physics of Fluids (1994-present)*, 14(6), 2002.
- [9] G. Haller and A.C. Poje. Finite time transport in aperiodic flows. *Physica D: Nonlinear Phenomena*, 119(34):352 – 380, 1998.
- [10] G. Haller and G. Yuan. Lagrangian coherent structures and mixing in two-dimensional turbulence. *Phys. D*, 147:352–370, Dec 2000.
- [11] George Haller. Distinguished material surfaces and coherent structures in three-dimensional fluid flows. *Physica D: Nonlinear Phenomena*, 149(4):248–277, 2001.
- [12] George Haller. A variational theory of hyperbolic lagrangian coherent structures. *Physica D: Nonlinear Phenomena*, 240(7):574–598, 2011.
- [13] George Haller and Themistoklis Sapsis. Lagrangian coherent structures and the smallest finite-time lyapunov exponent. *Chaos: An Interdisciplinary Journal of Nonlinear Science*, 21(2):023115, 2011.
- [14] C. S. Harrison and G. A. Glatzmaier. Lagrangian coherent structures in the California Current System - sensitivities and limitations. *Geophysical and Astrophysical Fluid Dynamics*, 106:22–44, October 2010.
- [15] CH Hsieh, ZP Jin, D Marthaler, BQ Nguyen, DJ Tung, AL Bertozzi, and RM Murray. Experimental validation of an algorithm for cooperative boundary tracking. In *Proc. of the 2005 American Control Conference.*, pages 1078–1083, 2005.
- [16] M.A. Hsieh, E. Forgoston, T.W. Mather, and I.B. Schwartz. Robotic manifold tracking of coherent structures in flows. In *Robotics and Automation (ICRA), 2012 IEEE International Conference on*, pages 4242–4247, May.

- [17] T. Inanc, S.C. Shadden, and J.E. Marsden. Optimal trajectory generation in ocean flows. In *American Control Conference, 2005. Proceedings of the 2005*, pages 674 – 679, 8-10, 2005.
- [18] Dennis Larkin, Matthew Michini, Alexandra Abad, Stephanie Teleski, and M Ani Hsieh. Design of the multi-robot coherent structure testbed (mcoste) for distributed tracking of geophysical fluid dynamics. In *ASME 2014 International Design Engineering and Technical Conference*. American Society of Mechanical Engineers, August 2014.
- [19] Francois Lekien, Chad Couillette, Arthur J. Mariano, Edward H. Ryan, Lynn K. Shay, George Haller, and Jerry Marsden. Pollution release tied to invariant manifolds: A case study for the coast of florida. *Physica D: Nonlinear Phenomena*, 210(12):1 – 20, 2005.
- [20] K. Mallory, M. A. Hsieh, E. Forgoston, and I. B. Schwartz. Distributed allocation of mobile sensing swarms in gyre flows. *Nonlinear Processes Geophysics*, 20(5):657–668, 2013.
- [21] M. Michini, M. A. Hsieh, E. Forgoston, and I. B. Schwartz. Experimental validation of robotic manifold tracking in gyre-like flows. In *IEEE International Conference on Intelligent Robots and Systems (IROS 2014)*, June 2014.
- [22] M. Michini, M.A. Hsieh, E. Forgoston, and I.B. Schwartz. Robotic tracking of coherent structures in flows. *Robotics, IEEE Transactions on*, PP(99):1–11, 2014.
- [23] M. Michini, H. Rastgoftar, M. A. Hsieh, and S. Jayasuriya. Distributed formation control for collaborative tracking of manifolds in flows. In *IEEE American Control Conference (ACC 2014)*, June 2014.
- [24] Matthew Michini, Kenneth Mallory, Dennis Larkin, M Ani Hsieh, Eric Forgoston, and Philip A Yecko. An experimental testbed for multi-robot tracking of manifolds and coherent structures in flows. In *ASME 2013 Dynamic Systems and Control Conference*, pages V002T32A002–V002T32A002. American Society of Mechanical Engineers, 2013.
- [25] H. E. Nusse and J. A. Yorke. A procedure for finding numerical trajectories on chaotic saddles. *Physica D Nonlinear Phenomena*, 36:137–156, jun 1989.
- [26] T. Peacock and G. Haller. Lagrangian coherent structures: The hidden skeleton of fluid flows. *Physics Today*, 66(2):41–47, 2013.
- [27] H. Rastgoftar and S. Jayasuriya. Preserving stability under communication delays in multi agent systems. In *Proceedings of the ASME Dynamic Systems and Control Conference (DSCC)*, 2013.
- [28] H. Rastgoftar and S. Jayasuriya. Evolution of multi agent systems as continua. *To appear in ASME Journal of Dynamic Systems, Measurement, and Control*, 2014.
- [29] Hossein Rastgoftar. Planning and control of swarm motions as continua. Master’s thesis, University of Central Florida, Orlando, Florida, USA, 2013.
- [30] Hayder Salman, Jan S Hesthaven, Tim Warburton, and George Haller. Predicting transport by lagrangian coherent structures with a high-order method. *Theoretical and Computational Fluid Dynamics*, 21(1):39–58, 2007.
- [31] Joseph T Schaefer and Charles A Doswell III. On the interpolation of a vector field. *Monthly Weather Review*, 107(4):458–476, 1979.
- [32] C. Senatore and S.D. Ross. Fuel-efficient navigation in complex flows. In *American Control Conference, 2008*, pages 1244 –1248, june 2008.
- [33] Shawn C. Shadden, Francois Lekien, and Jerrold E. Marsden. Definition and properties of lagrangian coherent structures from finite-time lyapunov exponents in two-dimensional aperiodicflows. *Physica D: Nonlinear Phenomena*, 212(34):271 – 304, 2005.

- [34] Stale A. Skogstad, S. Holm, and Mats Hovin. Digital iir filters with minimal group delay for real-time applications. In *Engineering and Technology (ICET), 2012 International Conference on*, pages 1–6, 2012.
- [35] S.H. Strogatz. *Nonlinear Dynamics And Chaos*. Studies in nonlinearity. Sarat Book House, 2007.
- [36] S. Susca, S. Martinez, and F. Bullo. Monitoring environmental boundaries with a robotic sensor network. *IEEE Trans. on Control Systems Technology*, 16(2):288–296, 2008.
- [37] Ioana Triandaf and Ira B. Schwartz. A collective motion algorithm for tracking time-dependent boundaries. *Mathematics and Computers in Simulation*, 70:187–202, 2005.
- [38] Jeffrey M. Walls and Ryan M. Eustice. An origin state method for lossy synchronous-clock acoustic navigation. In *IFAC Workshop on Navigation, Guidance and Control of Underwater Vehicles*, volume 3, pages 56–62, Porto, Portugal, April 2012.
- [39] Sarah E. Webster, Jeffrey M. Walls, Louis L. Whitcomb, and Ryan M. Eustice. Decentralized extended information filter for single-beacon cooperative acoustic navigation: Theory and experiments. *IEEE Transactions on Robotics*, 29(4):957–974, August 2013.
- [40] Weizhong Zhang, T. Inane, S. Ober-Blobaum, and J.E. Marsden. Optimal trajectory generation for a glider in time-varying 2d ocean flows b-spline model. In *Robotics and Automation, 2008. ICRA 2008. IEEE Int. Conf. on*, pages 1083 –1088, may 2008.